CHARACTERIZATION AND OPTIMIZATION OF UAV POWER SYSTEM FOR AERIAL AND SUBMERSIBLE MULTI-MEDIUM MULTIROTOR VEHICLE

by

PARTH V. SONI

A thesis submitted to the

Graduate School – New Brunswick

Rutgers, The State University of New Jersey

In partial fulfillment of the requirements

For the degree of

Master of Science

Graduate Program in Mechanical and Aerospace Engineering

Written under the direction of

Professor Francisco Javier Diez-Garias

And approved by

_____

_____

_____

New Brunswick, New Jersey

October, 2016

ABSTRACT OF THE THESIS

Characterization and Optimization of UAV Power System for Aerial and Submersible Multi-Medium Multirotor Vehicle

by Parth V. Soni

Thesis Director:
Professor Francisco Javier Diez-Garias

Even as an emerging technology, Unmanned Aerial Vehicles (UAVs) have had a tremendous impact on the world. From the way wars are fought, to the way we take selfies, drones are well on their way to revolutionizing our daily lives. One of the most innovative applications of these vehicles in the Naviator submersible-UAV. This unique multirotor is capable of aerial flight and underwater operations with seamless Air-Water transitions. In this thesis, the power system of a multirotor UAS is characterized using standard performance models with the goal of designing and optimizing the systems of a new Naviator V5 prototype. Test beds were created to collect data on BLDC motors and propellers and their performance was assessed in air and water. Theoretical models using BEM theory and the 3-constant motor model were validated for their accuracy. Experiments found that RC air propellers are similarly efficient in air and water and BLDC motor performance is partially diminished due to the higher viscosity of water. The effects of input voltage, throttle, Kv rating, and motor size were also evaluated using motor torque curves. Using this data, an optimal power system for the Naviator V5 prototype was designed, tested, and evaluated.

ACKNOWLEDGEMENTS

I would like to thank Professor Diez for letting me pursue this project from its inception. You have provided guidance for my research, supported my efforts, and pushed me to be the best I can be. I will always remember the lessons I've learned from you, and keep them in mind moving forward.

I would like to thank my all my friends and colleagues at Rutgers University especially Arturo Villegas and Marco Maia. Arturo, your aerodynamics advice and expertise in mathematical modeling was invaluable in completing this thesis. Marco, our collaboration on the Naviator has been one of the biggest learning experiences of my career and your broad skillset was immeasurably helpful in this project.

My biggest thank you is to my family. My parents have loved me and supported me through all of my endeavors. Thank you for helping me with my life, for raising me right, for teaching me all the things you've taught me, for making me the person I am today, and for so much more. I would also like to thank my grandparents for teaching me the value of what I have and making my days memorable. Lastly, I would like to thank my sister for her amazing curiosity and imagination. You asked the tough questions, forcing me think about the world in a new way, and inspired me in so many ways.

Table of Contents

List of Tables and Figures

1. Introduction

The first multirotors had been around for almost as long as fixed-wing aircraft. However, due to their mechanical complexity and high pilot workload, most work in these vehicles was abandoned until the 1950's. During this time, interest was renewed by the Cold War for an aircraft with greater maneuverability and hovering capability. Many manned experimental aircraft were built and while some succeeded into fully-fledged production models, they were more hybrids (such as a hover plane or twin-rotor helicopter) than true quadcopters. Again, interested waned in these projects until 5 decades later. In the early 2000's, a culmination of many technologies brought about the drone revolution that we see today. The introduction of cheap, reliable, powerful, and lightweight brushless motors in the 1980's provided the power plant for a modern quadcopter. The second electronics revolution brought about control electronics that could easily regulate the precise power delivery to these motors. Finally, the invention of high capacity, high discharge lithium-polymer batteries in the late 1990's provided the perfect power source for a small UAV. With modern electronics such as MEMS sensors and a little ingenuity, RC hobbyists revived the old quadcopter and brought it into the modern age. The simplicity, maneuverability, and low cost of a quadcopter attracted many manufacturers and the market soon exploded with interest. Today, multirotors are being used as research platforms, for aerial photography, delivering packages, and as search-and-rescue drones around the world.

1.1. History of Multi-Rotor Development

After the historical first flight of the Wright brothers, aviators immediately realized the complications that arose with a flying machine that required long stretches of straight, flat, unobstructed runways to land and take-off. Only 4 years after the first flight of the Wright Flyer in 1903, the Breguet brothers made an experimental rotorcraft with Vertical Take-Off and Landing (VTOL) capabilities. The Gyroplane No. 1, the world's first quadcopter, managed independent take-off but suffered from extreme instability [1]. During the next decade, other researchers such as Etienne Oemichen (Figure 1a) and Dr. George de Bothezat (Figure 1b) improved the structural design, engine power, and mechanics of the quadcopter to be able to perform flights as long as one kilometer. These design breakthroughs, which are still used today, made the first quadcopters into a viable flying machine [2]. The quadcopter was designed to hover by producing equivalent thrust from each of its four rotors. While the rotors produce enough total thrust to hover, each of the propellers will always be slightly different from each other. This meant that even when running all the rotors at the same speed, a quadcopter would always be intrinsically unstable. To produce stable flight, the RPM of each of the motors would have to be precisely controlled to stabilize the vehicle. Without computers, this method of control, while viable, places a monumental workload on the pilot making quadcopters impractical.

The advent of jet propulsion and the Cold War arms race renewed interest in the development of VTOL aircraft. Various powered lift concepts such as tail-sitters, quadcopters, tiltrotors, and vectored thrust were explored by the military using many experimental aircraft. Tail-sitter designs such as the Pogo (Figure 1c) were investigated

and abandoned due to the awkward position of the pilot during landing and take-off [3]. Quadcopter designs such as the X-19 (Figure 1d) and X-22 (Figure 1e), while innovative, suffered from power distribution problems as well as the persistent control issues that plagued quadcopters since their inception [4]. Of the hundreds of experimental aircraft, the Hawker Siddeley Harrier (Figure 1f) emerged as the only truly successful VTOL design of the Cold War. However, this unforgiving aircraft required exceptional pilots with extensive helicopter training and even then, more than half of the first generation planes crashed [5]. Around the same time, the military began creating programs for the development of Unmanned Aerial Vehicles (UAV's). Similar interests developed in the commercial and civilian sectors and led to the development of the Draganflyer (Figure 1g) in 1998 [6]. This unique design drew on elements of earlier projects, miniaturized the design, and supplied a platform for the development of the UAV flight controller. After capturing the attention of the RC community, amazing advances were made driven by the community and company partners that led to the DJI Inspire 1 (Figure 1h), the current state-of-the-art in multirotor technology [7].

1.2. Introduction of the UAV Flight Controller

The device that solved the century old problem of quadcopter instability was the UAV Flight Controller (FC). The invention of the FC was facilitated by two emerging technologies; the Micro Electro-Mechanical Systems (MEMS) that led to the development of micro-sensors capable of detecting inertial forces, and the proliferation of easy to program, single board microcontrollers like the Arduino. These technologies introduced unparalleled prototyping capabilities into the hands of developers and hobbyists. Internet communities formed to cooperatively develop open-source hardware

and software such as MultiWii, OpenPilot, and ArduCopter [8]. These cheap, reliable, single board flight controllers are what triggered the drone revolution we see today.

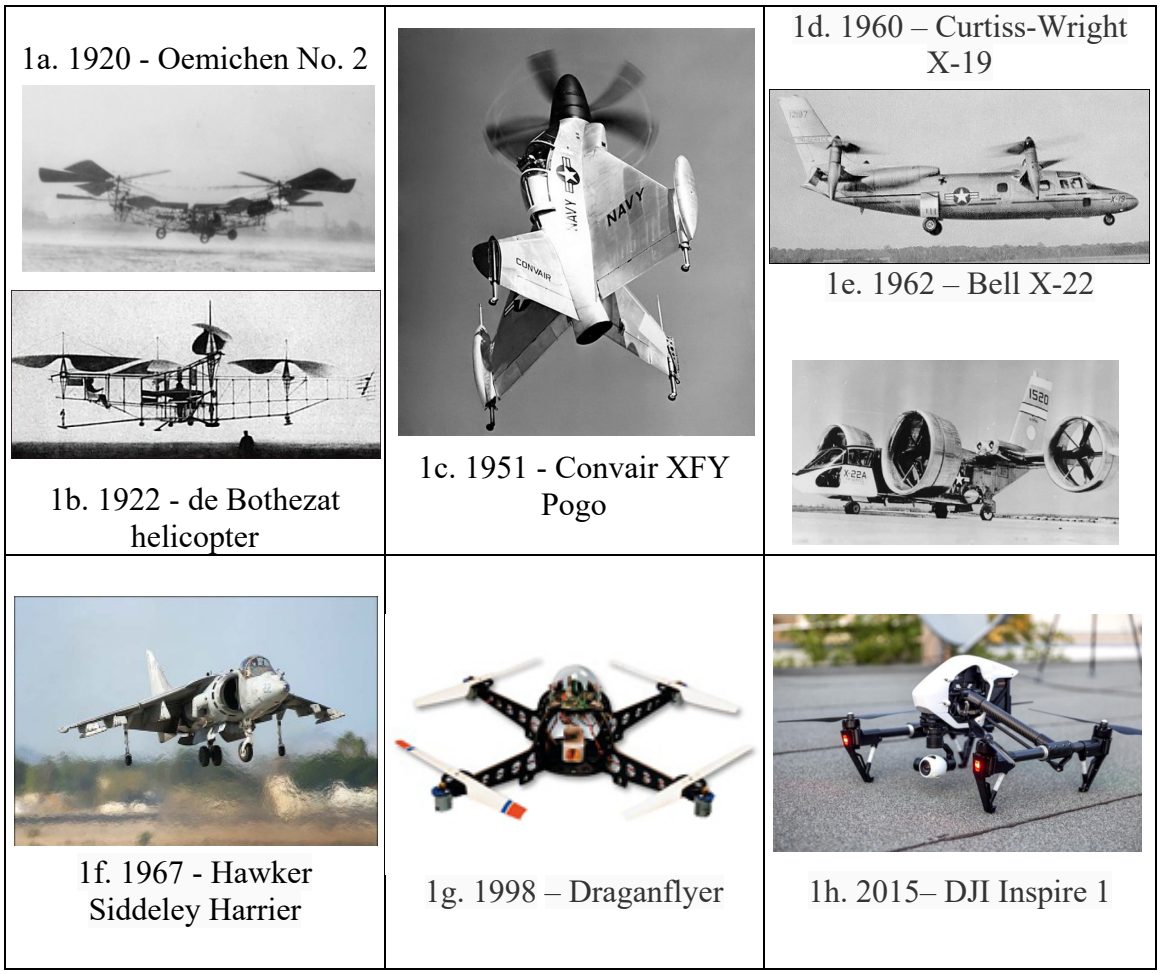

Figure 1a – 1h. Chronological development of the VTOL platform which led to the modern quadcopter

The core of a quadcopter's Flight Controller is the Inertial Measurement Unit (IMU). This integrated circuit contains the MEMS gyroscopes and accelerometers used for tracking the orientation of the vehicle. More advanced flight controllers also incorporate data from MEMS magnetometers, barometers, and GPS sensors for better accuracy. While each of these sensors have gaping fallacies like sensor drift, susceptibility to vibrations, environmental interference, slow response time, and thermal

or temporal degradation, a technique called sensor fusion can be used to correct for each sensor's inherent faults [9]. Sensor fusion takes measurement inputs from each sensor, applies digital filtering algorithms such as the Kalman filter to compensate for each other's deficiencies, and outputs accurate and dynamic positioning data [10].

Figure 2a shows a block diagram of a mainstream modern flight controller, the Ardupilot APM 2.5 (figure 2b). This FC contains all the major components, sensors, interfaces and communication protocols required to create an autonomous UAV multirotor in a compact and easy-to-use platform. This all-in-one flight controller supports data logging, ground station telemetry, and external sensors such as sonar and laser rangefinders. Founded by a thriving open-source developer community, integrating advanced sensors such as a barometer and magnetometer, as well as the capability to expand using standard communication protocols such as I^2C and UART, this popular controller has pioneered many of the features we see in autonomous multirotors today. With its broad codebase and advanced features, the ArduCopter APM was the FC of choice in the case study of this thesis, the submersible-UAV Naviator multirotor.

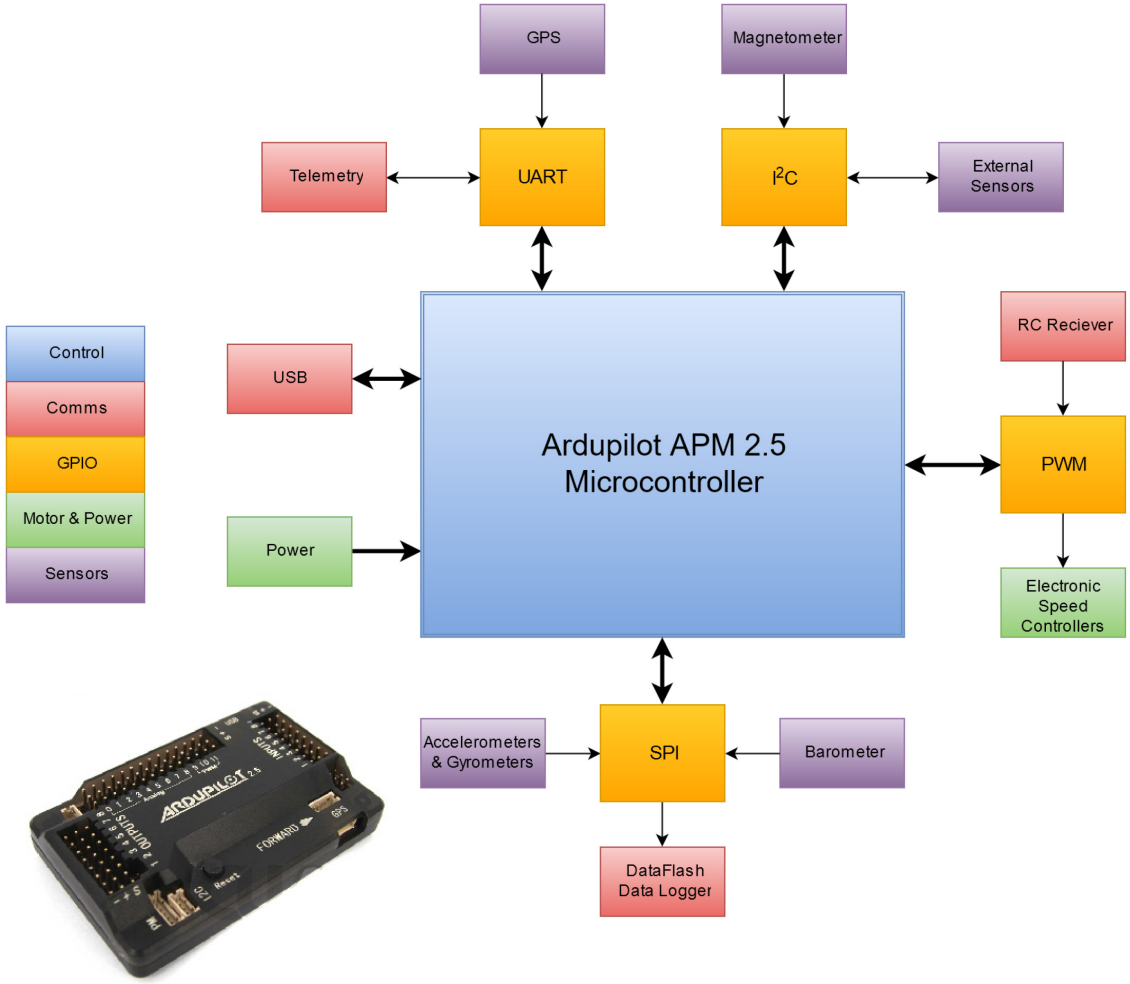

Figure 2a. Anatomy of the Ardupilot Flight Controller
Figure 2b. Ardupilot 2.5: An Integrated Open-Source Flight Controller for RC Multirotors, Helicopters, Planes, Cars & Boats developed by Open-Source Developers and 3DRobotics.

1.3. Quadcopter Flight Dynamics

Even though a quadcopter knows its attitude and position using the FC, quadcopter control is still a fundamentally difficult problem. A quadcopter has 6 Degrees-Of-Freedom (DOF), 3 translational and 3 rotational, but only has 4 independent inputs, the rotor speeds of each motor [11]. This results in a severely underactuated,

nonholonomic system in which two of the rotational and translational motions are coupled to achieve 6 DOF control [12]. The simple schematic in Figure 3 shows that in the quadcopter's case, forward and reverse translation is coupled with pitch, requiring forward pitch to advance forward and vice versa. Similarly, leftward and rightward translation requires rolling the vehicle in the corresponding direction. Altitude is adjusted by increasing or decreasing equal thrust to all four rotors to go up or down respectively. Finally, yaw is induced by mismatching the balance in torques between the counter-rotating pairs of motors. All of these dynamic motor manipulations are only possible with the aid of an Electronic Speed Controller (ESC). The ESC is a standalone electronic

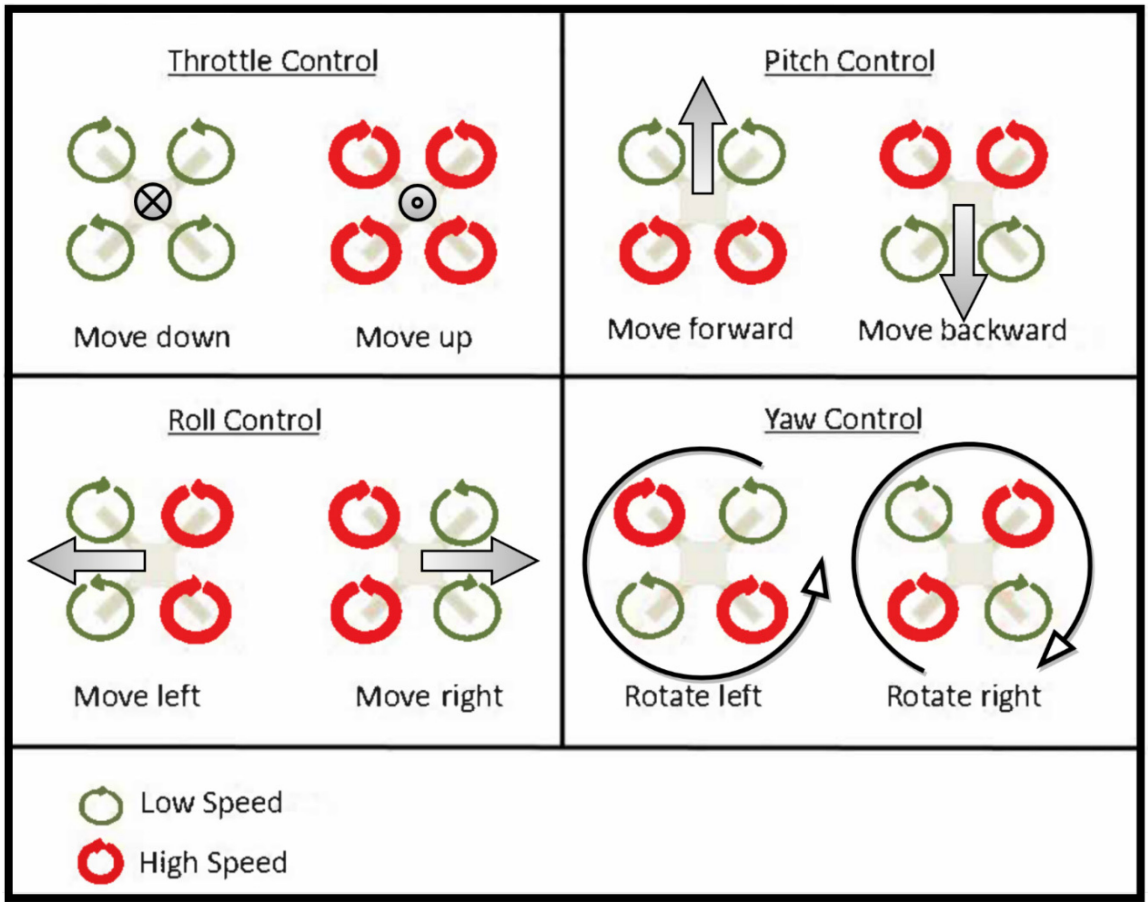

Figure 3. Quadcopter Flight Dynamics

commutation unit that interprets control signals from the flight controller and varies the motor commutation rate to control the electric motor's precise angular velocity.

1.4. Multirotor Applications

The development of quadcopters was unlike any other in history. Whereas theory and calculations lead building of a prototype, the quadcopter was created by RC enthusiasts through trial-and-error and the collaboration of thousands of people over the internet. For this reason, one of the first applications of the quadcopter was the modelling of its own behavior. Researchers used early quadcopters to create models using control theory and later began augmenting them with more advanced control schemes, range sensors, and cameras [13]. New scientific journals around UAVs formed with publications that began using UAVs as pioneering research platforms [14] [15]. Quadcopters also began to be used for aerial photography by non-technical consumers and amateur cinematographers. Billion dollar companies like DJI formed from the rapid expansion of the drone market. Giants such as Google, Amazon, and Facebook are creating drones for cargo transport and flying internet hubs. New drone racing leagues have also established a presence in the hobby market. Even with all these innovative applications, experts still agree that the full potential of drones has not even begun to be realized [16].

1.5. Development of UAV Power Systems

The UAV flight controller was the disruptive invention that launched the drone industry, but the enabling technologies that brought about its success lie in the systems

that power modern drones. Innovations in motors, speed controllers, RC propellers, and batteries are what built the foundations of the modern quadcopters.

1.5.1. BLDC Motors & ESCs

Brushless motors were invented in the 1960's for use in spacecraft during the Space Race. Early sounding rocket experiments showed that brush wear reduced the operational life of conventional brushed DC motors to a few minutes in the hard vacuum of space. This generated a great need for an efficient, reliable, long-life DC motor and in 1962, Kearfott Products created the first experimental brushless DC (BLDC) motor along with the solid state transistor circuitry required for practical commutation of the motor. Just three years later, space-qualified BLDC motors were used in the Apollo Lunar Module and Saturn launch vehicles. Unfortunately, while reliable, these early motors were not very powerful and the control circuitry was sophisticated, expensive, and required sensors positioned inside the motor to function [17].

In the 1970's, widespread use of integrated circuits drastically reduced the cost of the motor control circuitry. Tiny circuit chips that could fit inside the motor casing were introduced containing all the hall sensors, amplifiers and control logic circuitry needed to run the motor. Field Effect Transistor (FETs) switches capable of handling high motor currents were also incorporated into the circuit and gave rise to the modern Electronic Speed Controller (ESC). Over time, newer control schemes like back-EMF sensorless control completely removed the need for any sensors inside the motor, indefinitely extending the lifetime of a motor. Meanwhile, the invention and incorporation of neodymium magnets, the strongest and most affordable type of rear-earth magnets to date, in motor construction significantly increased power capabilities of BLDC motors.

With these technologies, new BLDC motors were developed that could fit in the palm of a person's hand and produce Kilowatts of efficient power.

1.5.2. The Lithium Polymer Battery

The final component that greatly aided the success of the quadcopter is Lithium-Polymer battery (Li-Po). Li-Po batteries are an evolution of lithium-ion rechargeable batteries in a pouch format. Since their commercialization in 1998, they have dominated the UAV market because of their compact size, high energy density, and fast discharge rates. Unfortunately, these cells suffer from all the same problems as any other lithium based battery. Conditions such as overcharge, over-discharge, over-temperature, and short-circuits can lead to pouch swelling, toxic electrolyte leakage, spontaneous fire, or even explosive failure. In addition, unlike lithium-ion cells that are contained in a hard case, Li-Po batteries only have a thin polymer casing making them susceptible to crush and nail penetration. Many examples can be found on the Web where a damaged Li-Po battery has burst into flames causing catastrophic damage to its surroundings. Despite these concerns, by following well established handling and charging techniques, most Li-Po batteries are relatively safe for use in UAV vehicles as compared to other power sources such as nitromethane or gasoline.

2. Theory

Understanding the power system of a multirotor requires a strong theoretical foundation in motor and propeller theory. In this section, blade element momentum theory is used to analyze propeller forces and torques. With this data, comparisons are drawn between BEM theory and experiments to determine its validity. As seen later on, predictions using BEM theory can be used to rapidly compare multirotor system options in any medium. On the other hand, motor theory provides a basis for motor behavior in air and water. The 3 constant motor model quantifies & explains the differences of a BLDC motor operating in air and water. It is also used to predict important operational points of the motor that are compared to experimental data to evaluate the model's accuracy.

2.1. Propeller Theory

Blade Element Theory (BEM) is a relatively simple method of predicting the performance of a propeller. The theory's framework was devised in the late 1870's and refined in the mid 1920's. As a result, it is a well-developed and widely used theory for propellers, turbines, and fans. Unfortunately, BEM theory neglects secondary effects such as radial flow caused by the rotation of the propeller or tip induced vortices which can lead to inaccuracies of 5% - 10%. Despite these inaccuracies, BEM theory is very useful for comparative studies and is still the best tool for generating predictions for thrust, torque, and efficiency of a propeller.

BEM theory models a propeller as a discrete set of 2-D blade elements as shown in Figure 4a. Each element is analyzed independently (Figure 4b) with the assumption

that there are only axial and tangential airflow velocity components (V_0 & V_2) and there is no radial airflow from one section to another. V_0 is a combination of the aircraft's forward velocity (U_∞) and the propeller's own induced axial flow. Similarly, V_2 is the combination of the blade section's angular velocity (Ωr) and induced tangential velocity of the fluid due to the acceleration around an airfoil. The induced axial and tangential effects can be approximated using their respective induction factors (a & a').

After calculating the local airflow velocity over the propeller (V_1 , $Eq.\ \{1\}$), the lift and drag forces can be calculated using standard lift and drag equations. The lift, drag, and inflow angle can be used to calculate the thrust and torque from this single element using equations $\{3\}$ and $\{4\}$. The local inflow angle (φ , $Eq.\{2\}$) is the difference between the geometric pitch angle (θ) and the angle of attack (α) at this section of the airfoil. Then, the overall thrust and torque can be found by summing the results of each individual blade elements. A more in-depth review of the theory is beyond the scope of this paper but more details can be found in other sources [18].

$$V_1 = \sqrt{(U_\infty(1+a))^2 + \left(\Omega r(1-a_t)\right)^2}\ ,\ \varphi = \theta - \alpha \qquad \{1\}\ ,\ \{2\}$$

$$\Delta T = \frac{N_b}{2}\rho V_1^2 c(C_L\cos(\varphi) - C_D\sin(\varphi)) * dr \qquad \{3\}$$

$$\Delta Q = \frac{N_b}{2}\rho V_1^2 c(C_L\cos(\varphi) + C_D\sin(\varphi))r * dr \qquad \{4\}$$

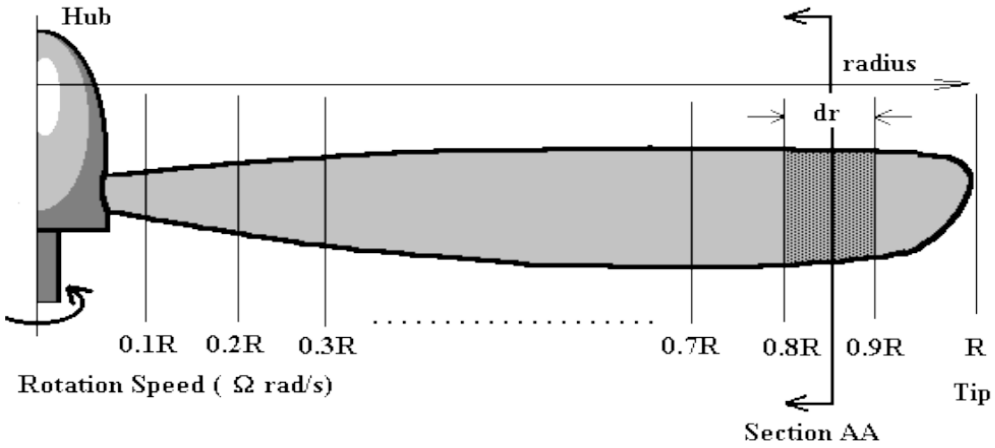

Figure 4a. Blade Element Subdivision using BEM Theory

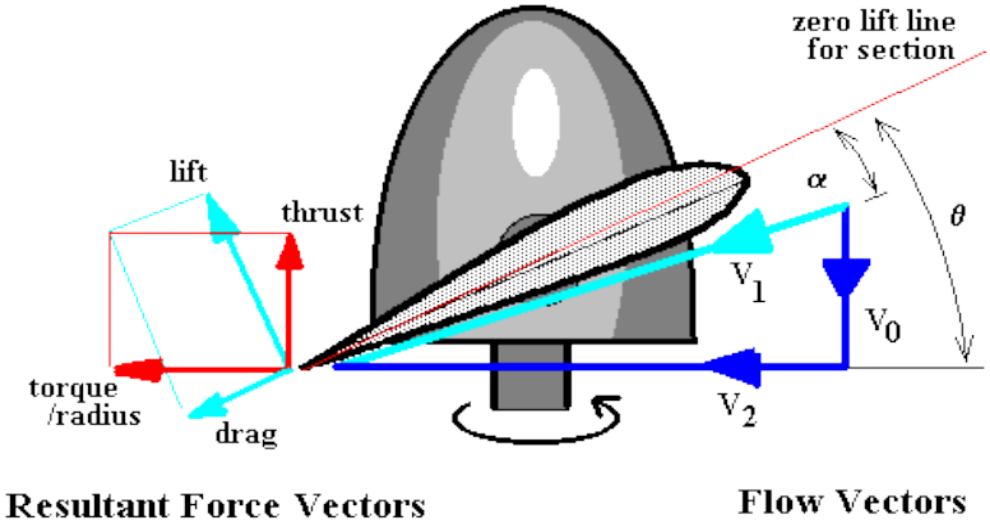

Figure 4b. 2-D Section Airfoil Analysis

In this paper, the results from BEM theory are used to analyze RC propellers in air and water. For a given RPM, we must calculate the thrust and torque produced by the propeller. Most manufacturers of RC propellers provide the diameter and pitch of propeller. As per the industry standard, this provided pitch (p) is assumed to constant over the whole blade. As per BEM theory, it is also assumed that the span-wise

distribution of chord, airfoil shape, and twist angle remains the same in all test conditions (i.e. the blade is a rigid body).

The chord distribution is assumed to be the same as the popular "Slow Flyer" propeller style due to the similarities in the overall propeller geometry. Other works have shown that this style of propeller maintains its chord profile even when the diameter and pitch are varied. This is probably due to the ease of manufacturing the same propeller profile in different sizes compared to creating different profiles for each specific size. These works have also produced detailed non-dimensionalized chord distribution curves which will be used for this analysis [19]. Some propeller manufacturers specify that their "Slow Fly" propellers are a blend of the NACA 4412, Clark Y, and Eppler E63 airfoils but don't specify their exact airfoil shape [20]. These types of airfoils are specifically designed for low Reynolds number operation ($0{\sim}100{,}000$). For these airfoils, a reasonable lift coefficient is $C_l = .85$, and a typical angle of attack for good performance is $\alpha = 8^o$ [21].

Due to the lack of any other manufacturer specifications, many other blade parameters must be estimated or assumed based on other sources. First, the Lift-to-Drag (L/D) ratio is estimated as $\frac{L}{D} = 6$, which is typical of rotorcraft propellers such as those on a quadcopter [22]. The $\frac{L}{D}$ ratio along with the lift coefficient results in a drag coefficient of $C_D = .14$. The axial (a) and tangential (a') induction factors are estimated to be $a = .3$ and $a' = .1$ [23] for realistic propeller operation. The final approximation stems from experimental data of an earlier Naviator V4 prototype. By varying the pitch angle of the vehicle, the Naviator can vary its flight speed from hovering to about 15 m/s

(35 mph). This means that its advance ratio can vary from $J \cong 0$ to $J \cong .5$. However, when the vehicle is tested in water, it maintains a steady forward speed. From previous experiments, the advance ratio in water is approximated to be $J \cong .3$. To make the calculations easier, the advance ratio is assumed to be same $J \cong .3$ for air and water.

None of these estimates change depending whether the vehicle is in air or water. The lift and drag coefficients are independent of the operating medium. The axial and tangential induction factors, and the angle of attack are only functions of the propeller. The advance ratio is assumed to be the same in both mediums. The only differences between air and water are the density and viscosity of the fluid.

2.2. Motor Theory

2.2.3. Fundamentals of Brushless Outrunner Motors

Motors convert electrical energy into mechanical energy using electromagnetic forces. Even if the operational theory may be different between different types of motors, this energy conversion is fundamentally the same in all electric motors. In the modern multirotor market, the dominant motor of choice is the sensorless, electrically commutated, three-phase, brushless direct current outrunner motor (BLDC outrunner). This motor is preferred because of its low cost, low maintenance, fast dynamic response, and high efficiency. However, all BLDC motors require a separate electronic speed controller (ESC) which commutates the input current to function properly. The ESC transforms DC power from a battery to 3-phase AC power using a network of field effect transistors (FET's). This AC electric signal is not restricted to a sinusoidal waveform; it

simply a bi-directional current so the electromagnetic stator coil can polarize as a N or S pole.

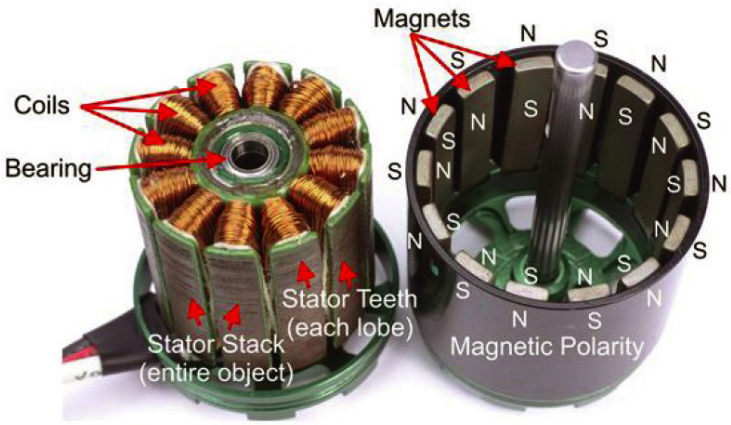

Figure 5. BLDC Outrunner Components

A BLDC motor is made up of only 2 major parts: the stator and the rotor [24]. The stator is the non-rotating central armature of the motor. The stator houses electromagnetic coils wrapped around a layered steel core. Each stator stack has stator teeth arranged in triplets to maintain the 3-phase winding symmetry. This means that matter how a BLDC motor is sized, its total number of stator coils must be multiples of three. The copper winding wire is laminated with a thin layer of polymer insulation to force current around the coils and generate the magnetic field. The outer rotor is made up of permanent neodymium magnets arranged with alternating polarities. The rotor always has an even number of magnets due to the number of available magnetic poles (North or South). It also has a central shaft that passes through the stator and is used to attach a propeller. Bearings on both ends of the motor provide a low friction surface and a c-clip on the shaft prevents it from being removed from the stator [25].

The operation of a BLDC is based on the force interaction between the permanent magnets on the rotor and the electromagnets in the stator. The motor goes through a cycle

of activity called an electrical rotation that is repeated to run the motor. From the point of reference of the magnet, this cycle starts when a magnet is directly above one of the coils of the stator. At this point, the ESC energizes the next coil ahead of the magnet such that it attracts the magnet. At the same time, the previous coil behind the magnet is energized with the opposite polarity to repel the magnet. This causes the magnet and rotor to turn towards the next coil. As the magnet approaches the next stator tooth, this coil is disconnected by the ESC and left floating. Again, the ESC energizes the next coil ahead of the magnet and the previous coil behind the magnet. This constitutes one electrical rotation from the point of reference of the magnet. From the point of one of the stator teeth, one electrical revolution is when the coil is energized to one polarity, then disconnected to float, re-energized to the opposite magnetic polarity, disconnected again, and finally energized to its starting polarity [26]. In a real motor, the arrangement of the coils in relation to the magnets is such that this cycle can be conducted on multiple coils of the motor. This produces more torque without increasing the size of the motor and affords finer motor control.

The key to controlling the sensorless BLDC motor is the back-EMF it generates. During rotation, the relative motion between the coils of the stator and the magnets of the rotor generates a voltage in the windings in accordance with Faraday's Law. Due to the arrangement of the coils, this induced voltage, called back-electromotive force (back-EMF) always opposes the input voltage in all the coils regardless of polarity. This phenomenon is directly related to the rotation speed of the motor, and causes the motor to act like a generator and a motor at the same time. As the motor speeds up, the induced counter-voltage increases reducing the original applied voltage. With a lower overall

voltage across the coils, the current flowing into the motor is also reduced [27]. As the power applied to the motor decreases, its acceleration begins to plateau to a constant velocity, the no-load operational point. Here, the applied voltage and the back-EMF are offset just enough so that the current flowing into the motor is exactly enough to overcome the air resistance and the resistivity of the copper coils. Conversely, when a motor decelerates, like when a load is placed on it, the back-EMF decreases allowing more total voltage and current into the coils. This increased current produces more torque in the motor thus bringing it to a constant but slower rotational velocity [28].

The back-EMF voltage is also how a ESC is able to determine the position of the BLDC rotor and select which coils to energize to maintain motor rotation. When a magnet is approaching the coil, the ESC disconnects the applied voltage to the coil and instead measures the voltage in the coil. The approaching magnet induces a positive back-EMF voltage in the coil. Then, as the magnet passes the top of the coil and begins moving away, it generates a negative back-EMF voltage. ESCs use a special circuit called a zero crossing comparator that determines precisely when the voltage switches from positive to negative. This is the precise time at which the permanent magnet is directly above the coil and the exact time to energize the coils ahead and behind the magnet with the correct polarities. This overview of the operation and control of a BLDC motor is sufficient groundwork for understanding the motor model that will be used in the next section.

2.2.4. 3-Constant BLDC Motor Model

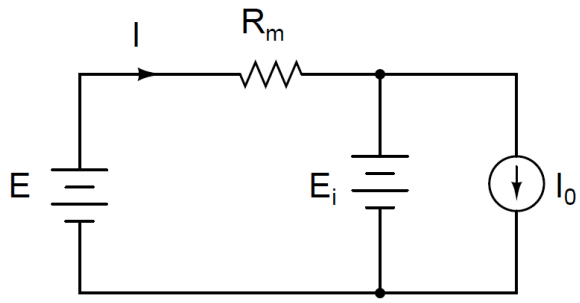

Figure 6. 3 Constants Motor Model

The traditional three constants model of a BLDC motor is shown in Figure 6. This model neglects the complex ESC that is required with all brushless motors; instead, it focuses on the operational energy losses of the motor. The first and simplest constant is R_m, the resistance of the copper motor windings to the flow of current. This is a fundamental quantity of any copper wire such as the magnet wire that makes up the motor coils. The next constant is I_0, the motor idle current of the motor at full throttle. I_o represents the energy lost due to bearing friction, air friction, and magnetic hysteresis in the motor. Modeling these losses would be an incredibly difficult challenge for a complex object such as a BLDC motor but fortunately, I_0 is very easy to measure. In addition, all these losses are linearly proportional to the motor's RPM which is proportional to the applied voltage. This means that a constant idle current is a good model for energy losses since the equation for electric power loss is also directly proportional to voltage [29].

$Complex\ motor\ losses \propto RPM \propto Voltage \propto Electric\ power\ losses$ and thus I_0 can be modelled as a constant for all applied voltages. The final constant in this model is K_v, the back-EMF voltage generated by the motor due to rotation. As discussed previously, this voltage acts as a resistance which reduces the applied voltage and opposes the current flow delivered to the windings. When the RPM of the motor

increases, the back-EMF increases which in turn resists the current flow in the windings decreasing current delivery to the armature. Vice versa, as RPM decreases such as when a load is applied, back-EMF decreases leading to more current flow the armature [30].

The 3-constant model of a motor is well defined for motors in air. It can be used to predict many of the important points on the torque curves of a BLDC motor. Applying Kirchhoff's voltage law to Figure 6, we find that:

$$E_i = E - IR_m \text{ , where } I \text{ is the input current , } E \text{ is the input voltage, } E_i \text{ is the backEMF } (effective) \text{ voltage, and } R_m \text{ is the winding resistance} \quad \{5\}$$

During normal operation, the motor must always overcome its internal friction losses. This translates to wasted current that must be subtracted from the input current.

$$I_{eff} = I - I_0 \text{ , where } I_0 \text{ is the no-load current} \quad \{6\}$$

Using equations {5} and {6}, we can calculate the power output of the motor.

$$P_o = (E - IR_m)(I - I_0) \quad \{7\}$$

Next, the efficiency of the motor can be calculated using equation {8}

$$\eta = \frac{P_o}{P_{in}} = \frac{(E - IR_m)(I - I_0)}{EI} \quad \{8\}$$

However, when a BLDC motor is used in an underwater environment, some changes in the constants need to be accounted for. The first constant R_m is a variable of the copper windings of the motor. Since they remain the same and are insulated from the water by the lamination, this constant remains the same in air and water. I_0 is a measure of energy losses incurred by the motor due to external influences. This constant is

predicted to increase in a more viscous environment like underwater. Kv is a function of the number of turns in the coils of the motor and thus should also remain the same in both environments.

3. Experimental Setup

Modern multirotors are a relatively new development in the UAV industry. Unlike other civilian UAV's which were developed from industrial or military vehicles, modern multirotors were invented & developed by hobbyists & RC enthusiasts. In addition, most multirotor parts are made by Chinese manufacturers. As a result, multirotor data is scarce or non-existent. In this section, an overview of the experimental setup is presented that was used to thoroughly & quickly test multirotor motors & propellers. Initial testing was done in an aquarium tank using generic load cells to make measurements. However, larger propellers could not be tested due to limitations in size and boundary layer interactions. Testing was thus moved from the tank to the water tunnel. A fast and comprehensive data acquisition system was added to improve data collection. In addition, a sensitive torque sensor was added to the setup. To decouple motors and propellers, a motor test bed was created to separately test motors. This test bed was able to accumulate enough data to plot the entire torque curve of the motor.

3.1. Tank Test Bed

Preliminary testing for a RC system was done in a large 75-gallon aquarium tank. This setup measured RPM using an optical tachometer, thrust using a standard load cell, torque using standard load cell with a moment arm, voltage and current with a benchtop power supply, and throttle with a digital servo tester. A schematic of the setup is presented in Figure 7. To test the setup in air, the tank was simply removed and the system was tested in air. This setup was effective at testing multiple combinations of motors, propellers, and ESCs at various voltages.

The optical sensor is a standard digital laser tachometer model DT-2234C. Reflective tape was affixed to the rotor of tested motors to improve detection through glass and water. A generic 20Kg load cell paired with a HX711 load cell A/D converter was used to measure the thrust generated by the system. Another generic 5Kg load cell and HX711 load cell module with a 6 cm. moment arm was used as a torque sensor to measure the motor torque. An aluminum shaft freely able to rotate was used to transfer the thrust and torque from the motor and propeller to the load cells outside the tank. DC power was supplied using a Maiseng 50V/100A power supply calibrated using a Fluke 115 multimeter. The load cells were also calibrated using a precision brass weight set. Finally, the data from the sensors was collected using an Arduino Teensy 3.1 microcontroller.

A point of note for the remainder of the present study is that when efficiency of a BLDC motor is described, this efficiency includes the efficiency of the ESC as well. This is because power measurements between the ESC and motors is very difficult to measure. The ESC outputs are highly dynamic, 3-phase non-sinusoidal currents. Fortunately, it has been shown that the efficiency of brushless ESCs is very close to 100% for most of its operational range [31].

$$\eta_{sys} = \eta_{motor} * \eta_{ESC}\ ,\ but\ \eta_{ESC} \cong 1, so\ \ \eta_{motor} \cong \eta_{sys} \quad \{9\}$$

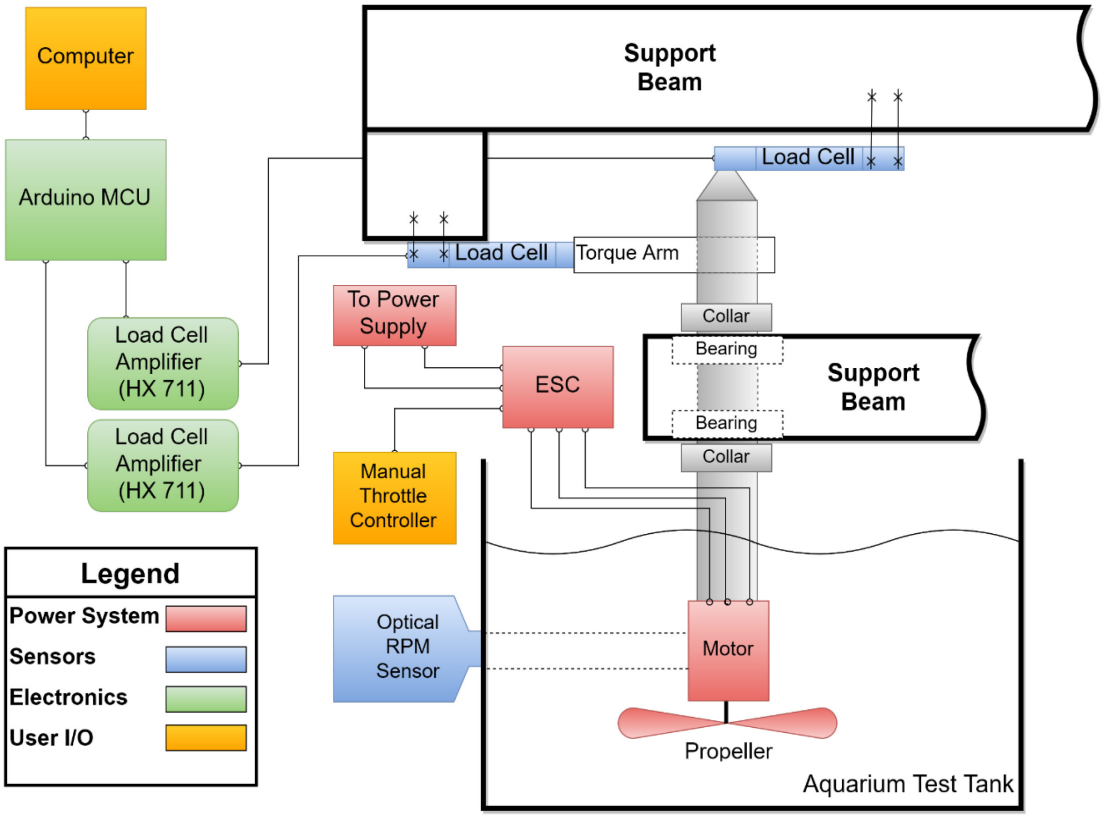

Figure 7. Aquarium Tank Test Bed

After establishing baseline performance parameters for select motors, the effects of corrosion resistant coatings on motor behavior was tested in the aquarium tank test bed. For these experiments, it was assumed that since the stator was made of metals such as copper and steel, coatings that enhance corrosion resistance of metals would protect BLDC motors as well. Control motors and coatings of WD-40, CorrosionX, and CorrosionX Heavy Duty were tested in tap water. Performance comparisons were done with each coating and visual inspections of the stator were done after prolonged exposure of each sample in water.

While the aquarium test bed worked well for most measurements, it was restricted to testing smaller propellers only. As propeller sizes were increased into 14” - 16” range, boundary layer interactions with the walls and recirculation around the tank became

significant error contributors. As a result, it was decided to move to the water tunnel for the remainder of the testing.

3.2. Motor Test Bed

To decouple the system and analyze its individual components, the BLDC motor, propeller and ESC must be tested separately. This is possible using a separate test bed for the motor but as shown in previous sections, a BLDC motor cannot operate without the electrical commutation of the ESC. For these experiments, the same ESC was used for testing all the motors.

For the motor test bed (Figure 8), some specialized components were purchased to produce accurate measurements. In this setup, the load cell and torque arm element was replaced using a Sensing Systems 1 N*m submersible torque sensor. The torque cell was factory calibrated using NIST traceable calibrations and the output data was conditioned using a standard HX711 A/D convertor [32]. A voltage and current sensor with Arduino output was also added to the system to streamline data collection. The optical tachometer was reused from the previous experiment but modified to provide a digital RPM output to an Arduino. All sensor data was output from the Arduino via the serial port. This setup was built in collaboration with Marco Maia and constituted as a fast and reliable data acquisition system that was reused with some modification in the water tunnel testing.

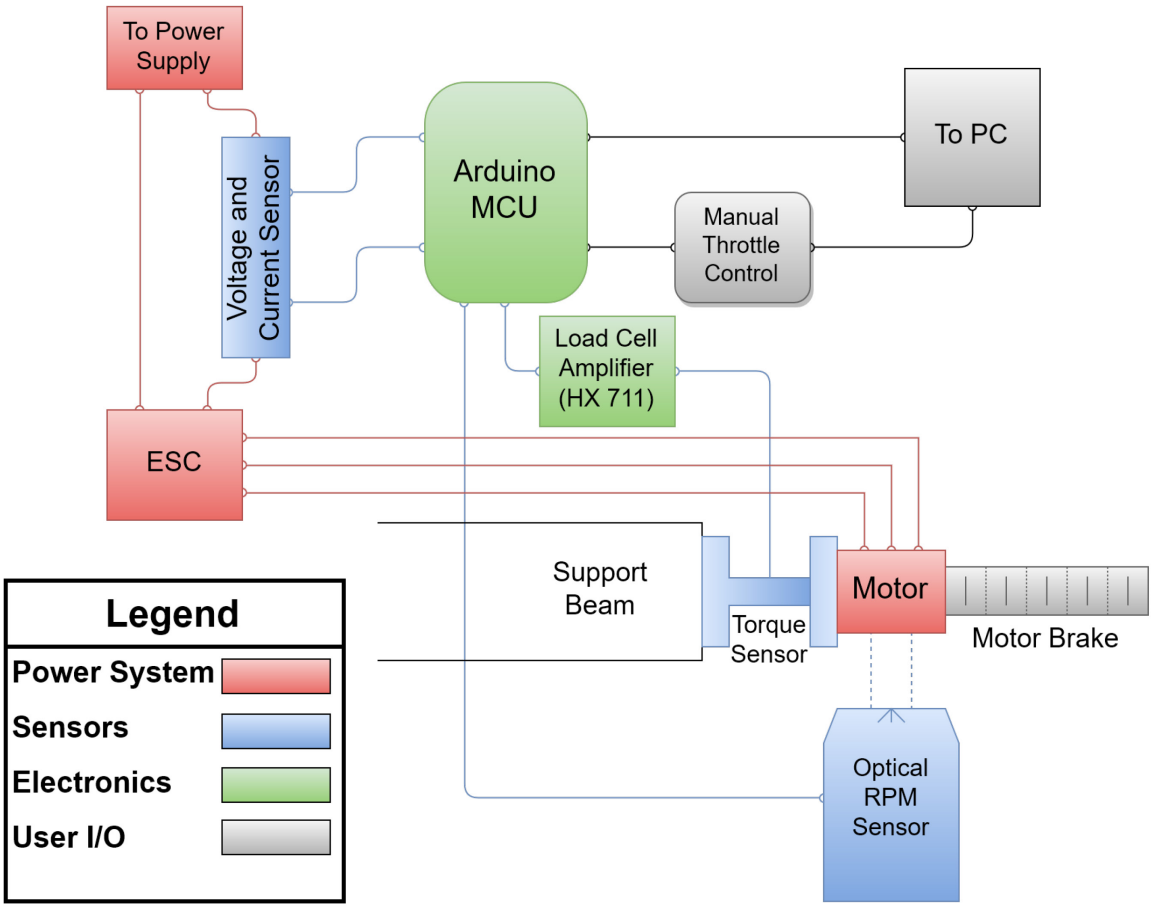

Figure 8. Motor Curve Test Bed Schematic

3.3. Water Tunnel Test Bed

The LEFTE lab water tunnel is a suitable location to test multirotor behavior in water. The tunnel offers a large cross-section, smooth laminar flow, and a range of flow rates for propeller testing. The flow in the water tunnel is generated using a large induction pump motor and is diffused by a honeycomb structure before entering the tunnel. When the tunnel was first set up, the flow speed in the tunnel at a height of 28" was mapped against the operating frequency of the induction motor. The tunnel was filled to a height of 22" to create a square cross-section for all water tunnel experiments. The

speed of the fluid flow for this height was calculated using the continuity equation for incompressible flows and the earlier calibration of the water tunnel.

The tunnel was run in 5 different conditions: empty, static water with no flow, and water flow at .1, .2, .3 m/s. The flow rate limit of this water tunnel is .3 m/s; the speed of the water tunnel was confirmed by releasing drops of food coloring and measuring the travel time of the drops over a 1m distance. This limit does not present a problem since the operating speed of the Naviator in water is only about .5 m/s. In the tunnel, the experiment was setup as shown in Figure 9. A generic 20Kg load cell was sealed using 2-part epoxy to permit underwater usage. The load cell was tested in agitated waters for an extended period of time to confirm its functionality and impermeability. Aluminum adapters were used in-between the load cell, torque cell, and motor to align them all along one central axis. Each sensor was connected to an Arduino Nano MCU using sealed coaxial cables to prevent interference from any ripple voltage that may leak from the motor into the water. The water tunnel was cleared of any obstructions prior to the propeller.

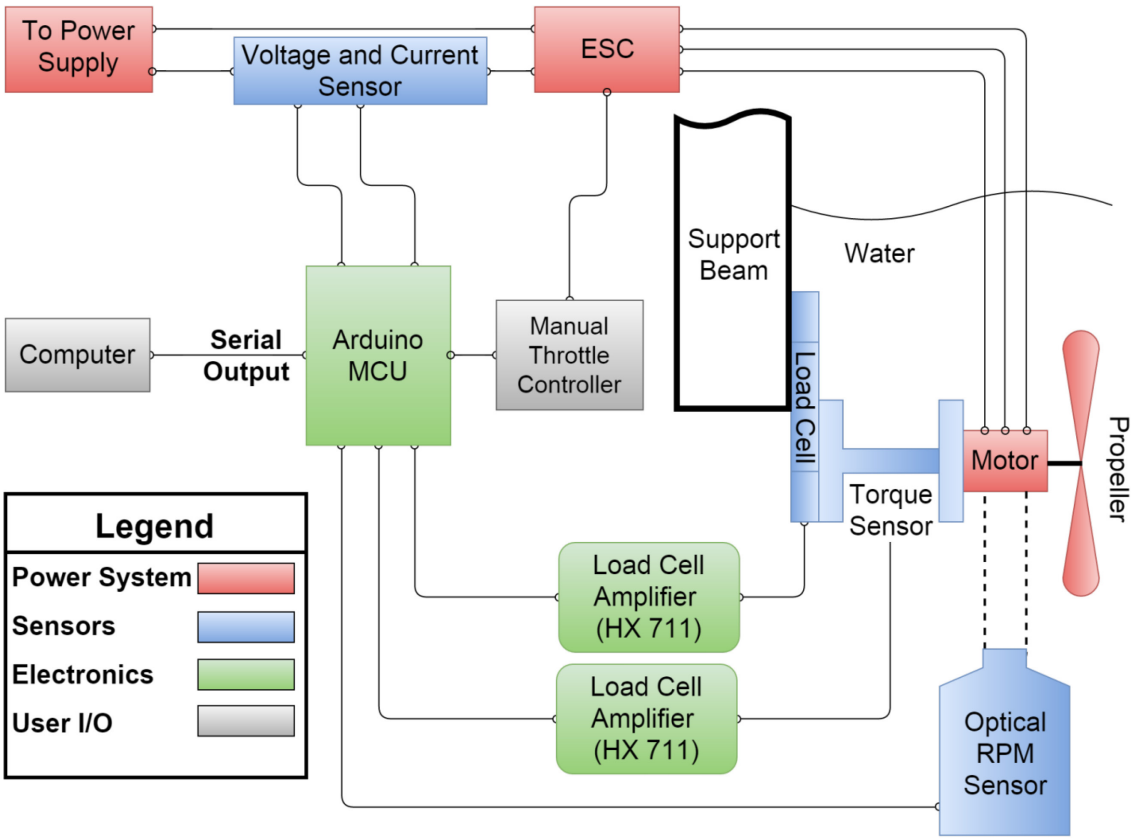

Figure 9. Water Tunnel Test Bed Schematic

3.4. Motors, Propellers, & ESCs Tested

A range of commercial RC motors, propellers, and ESCs were tested using the aforementioned experimental methods. ESCs from reputable manufacturers such as Castle Creations, T-Motors, KDE Direct, Turnigy, and Afro ESC were tested for functionality in water. However, all of these ESCs suffered from instabilities such as stuttering, stalling, overheating, or force resetting during underwater operation. Later, ESCs from generic manufacturers such as Hobbywing were tested and a ESC of suitable capabilities was found. This ESC was the only ESC used for all further testing and its specifications can be found in the appendix.

Most RC manufacturers label their motors based on their size and Kv rating. To understand the effects of different parameters on motor behavior in air and water, a range of motors were tested with Kv parameters ranging from 270Kv to 1000Kv and sizes ranging from 28mm to 40mm in diameter.

RC propellers are labelled based on diameter and geometric pitch. During initial testing propeller sizes ranged from 5" - 15". Propellers made from plastic and carbon fiber were tested but plastic propellers were prone to permanent deformation under high stress. Thus, all further testing was done using carbon fiber propellers whose diameter and pitch ranged from 8" – 15" and 3.3" – 5.5" respectively. Since RC propeller air performance data is available from some reliable peer-reviewed sources, comprehensive wind tunnel testing will not be pursued in the study. Instead, this study will focus more on the underwater behavior of the system.

4. Results & Discussion

In this section, the motor and propeller data analysis methodology is presented along with theoretical and experimental data comparisons. Then, by combining valid theoretical propeller predictions and experimental motor tests, operational points of motor propeller pairs are tabulated. A comparison between the available manufacturer & experimental data is also presented to highlight exaggerations in mfg. data. Next, the plausibility of using air motors and propellers in water was evaluated. Even with the limited available speeds of the test tunnel, experiments show that RC propellers are efficient in air and water. Motors were tested to determine the effects of various variables on performance parameters such as endurance and agility. A case study was performed with the goal of selecting an optimized power system for the Naviator S-UAV multirotor. Using the results of the experiments and analysis, appropriate motors, propellers, ESCs, and batteries were selected for the vehicle. The recommendations were experimentally verified and enhanced with other practical recommendations.

4.1. Methodology

4.1.1. Theoretical Analysis of Propellers

Propeller analysis was conducted by using the theoretical predictions of BEM theory and the experimental water tunnel test bed data. As stated in previous sections, the realistic estimations in Table 1 had to be made to be able produce meaningful calculations using BEM theory.

Air	Water
$\boldsymbol{\rho = 1.225\ \frac{kg}{m^3}}$	$\rho = 1000\ \frac{kg}{m^3}$
$\boldsymbol{\frac{L}{D} = 6}$, $\boldsymbol{C_L = .85}$, $\boldsymbol{C_D = .14}$	$\frac{L}{D} = 6$, $C_L = .85$, $C_D = .14$
$\boldsymbol{a = .3}$, $\boldsymbol{a' = .1}$	$a = .3$, $a' = .1$
$\boldsymbol{\alpha = 8^o}$, $\boldsymbol{J = .3}$	$\alpha = 8^o$, $J = .3$

Table 1. Realistic Assumptions of Some Aerodynamic Variables

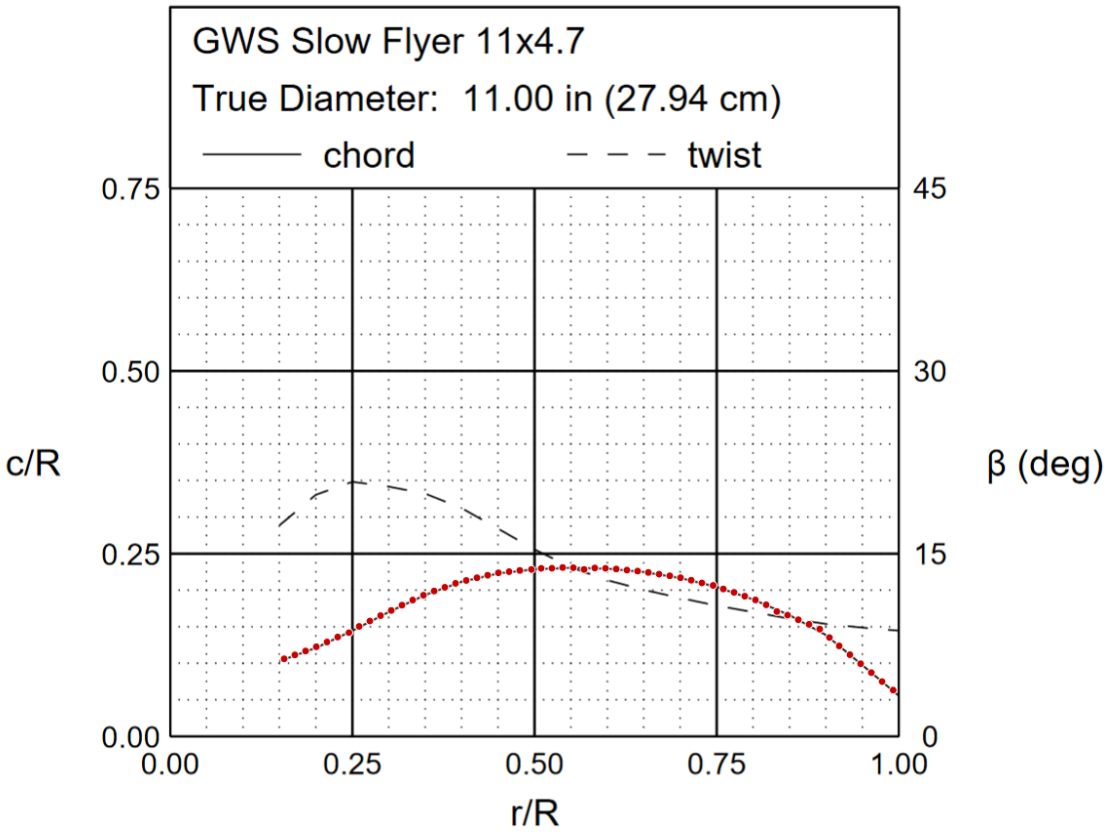

Figure 10. Chord Distribution Data Extracted from UIUC Propeller Database

The chord distribution was estimated from the University of Illinois RC propeller database using a GWS "Slow Fly" profile [33]. The graph was analyzed using WeplotDigitizer [34], a program that extracts data points (Figure 10) from curves on a graph. Using this data, the airfoil is divided into discrete n sections and each is analyzed as follows.

The procedure to calculate the thrust and torque curves of a propeller starts with figuring out the operational RPM range of the propeller. From some initial testing, it was found that the smallest (8") propeller with the largest motor (40 mm diameter) didn't exceed 10,000 RPM in air and 1,000 RPM in water. Thus, that was the range of RPM inputs (0 – 10,000 RPM in air, 0 – 1000 RPM in water) used for this calculation.

The calculation scheme used to build a database of propeller data is as follows. For each of the n sections of the airfoil, the subsequent BEM theory calculation is used to find the section thrust and torque at a specific RPM. Then, the section values are summed to find the total thrust and torque generated by this propeller at a specific RPM. Finally, the RPM is changed to the next value in sequence and the calculation repeated for all of the sections again.

First, the non-dimensional chord distribution is dimensionalized using a specific propeller radius (R) and pitch size (p). This constant pitch (p) is used to find the geometric pitch (θ) using the standard pitch equation {10}. In equation {10}, r is the radial distance to the current n^{th} section.

$$\theta = \tan^{-1}\left(\frac{p}{2\pi r}\right), \quad \varphi = \theta - \alpha \qquad \{10\}, \{11\}$$

Next, the advance velocity is calculated using the advance ratio (J) in equation {12}.

$$J = \frac{U_\infty}{nD}\ ,\ so\ U_\infty = J * n * D\ ,\ where\ D\ is\ the\ diameter\ of\ the\ propeller,$$

$$and\ n\ is\ the\ Revolutions\ Per\ Second \quad \{12\}$$

Then, the relative airflow velocity over the airfoil (V_1) is calculated using equation {13}.

$$V_1 = \sqrt{(U_\infty(1+a))^2 + \left(\Omega r(1-a_t)\right)^2}\ ,$$

$$where\ \Omega\ is\ the\ revolution\ rate\ in \frac{rad}{s} \quad \{13\}$$

Finally, with all other variables calculated, the section thrust and torque can be calculated with equation {14} and {15}.

$$\Delta T = \frac{N_b}{2}\rho V_1^2 c(C_L\cos(\varphi) - C_D\sin(\varphi)) * dr\ ,$$

$$where\ N_b\ is\ the\ number\ of\ blades\ of\ the\ propeller \quad \{14\}$$

$$\Delta Q = \frac{N_b}{2}\rho V_1^2 c(C_L\cos(\varphi) + C_D\sin(\varphi))r * dr\ ,$$

$$where\ c\ is\ the\ chord\ in\ this\ specific\ section \quad \{15\}$$

This procedure is repeated for each of the n sections, and the total thrust and torque is calculated by numerical integration using the trapezoidal rule. With the overall thrust and torque calculated for the complete airfoil, the RPM is changed for the next iteration until the full RPM range is calculated. Figure 11 shows the thrust and torque curves of a sample 12”x4” propeller in air and water. One notable difference in air and water operational range is the very low RPM required in water to produce the equivalent thrust as in air. After comparing some data points, theoretical curves show that at the same RPM, a propeller can produce about 30 times as much thrust in water as in air.

Next, the theoretical predictions are compared to the experiments in the water tunnel. To validate the water tunnel setup, the same experiment is done with two different motors. The motor specifications are not important in this experiment; since both setups use the same propeller, the data should lie on the on same propeller curve. The experimental data is plotted on Figure 12. Both experiments lie along the same curve and agree very well with the theoretical predictions. The theoretical predications are slightly higher that the experimental data and this is likely due to some minor errors in the assumed values or the losses that aren't accounted for in BEM theory. The assumptions, methodology, and calculation scheme used in this analysis was developed in collaboration with Arturo Villegas for the optimization of the Naviator prototype power system. Other experiments with the same methodology were also performed with different propellers and motors. They showed similar agreements between each experiment and the theoretical predictions.

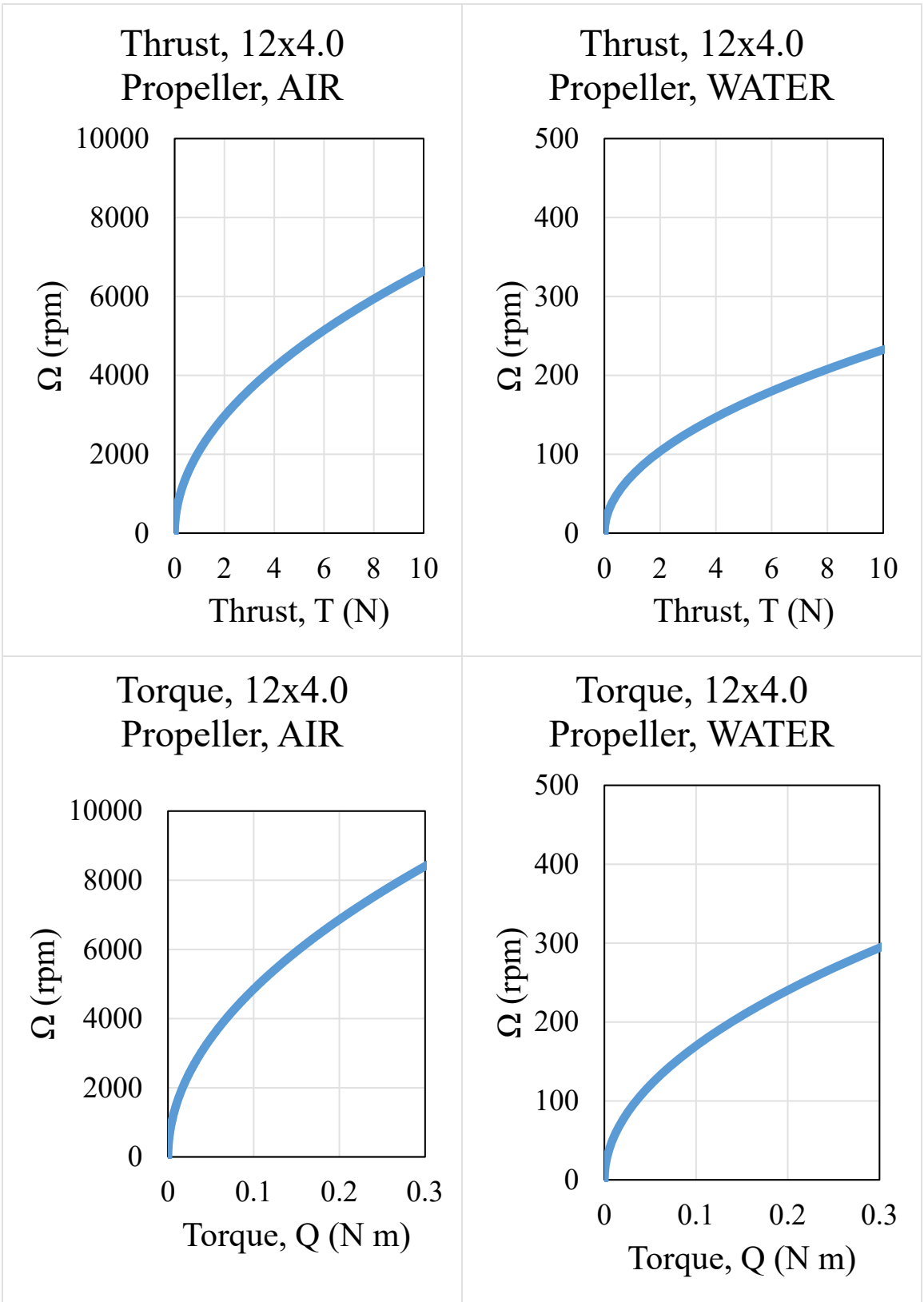

Figure 11. Theoretical Thrust and Torque Curves for a Propeller in Air and Water

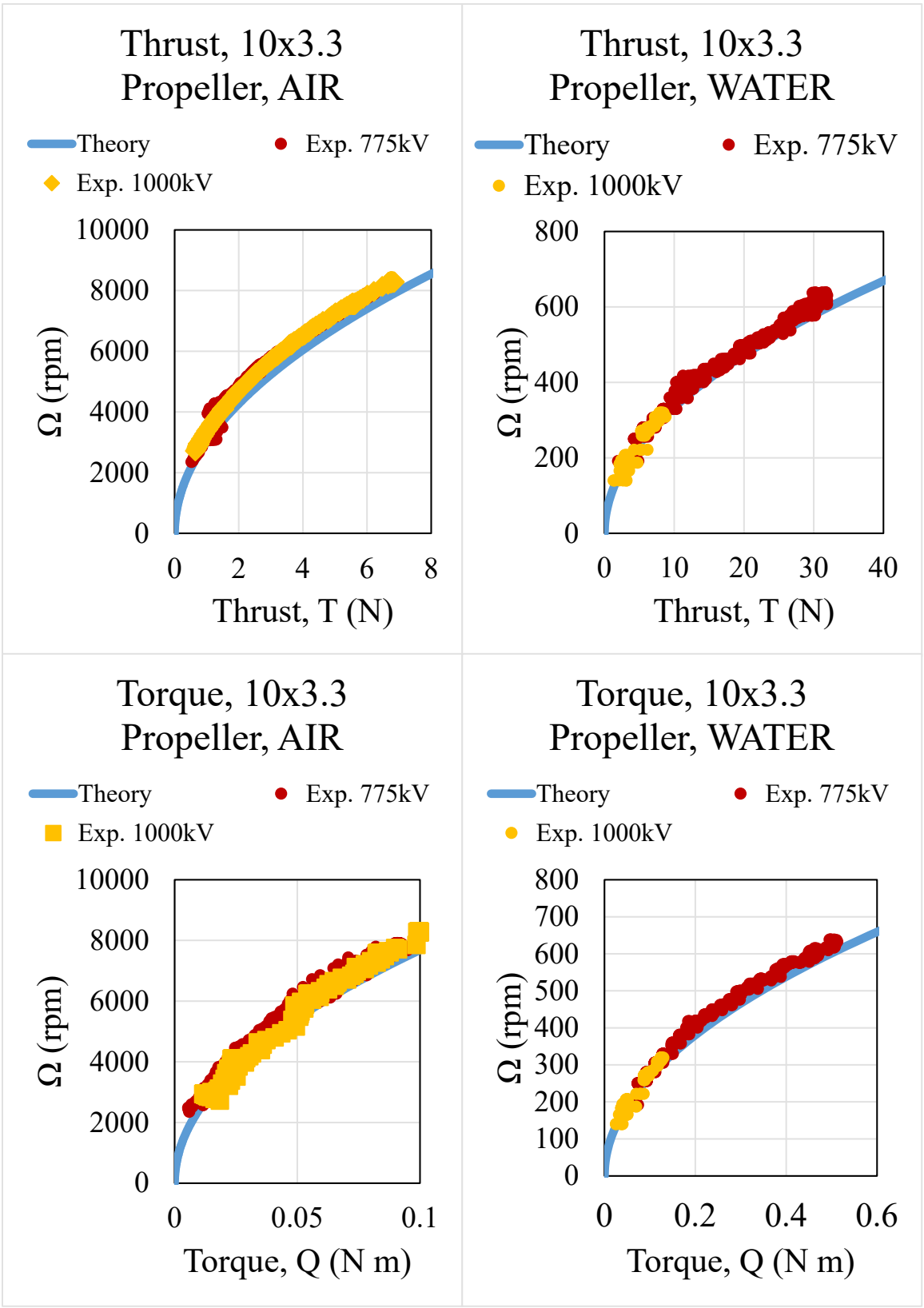

Figure 12. Comparison of Theoretical and Experimental Propeller Curves for 2 Different Motors and the Same Propeller.

4.1.2. Motor Curve Analysis

The BLDC motors were analyzed using characteristic motor curves such as the idealized curve shown in Figure 13. This sample curve shows many of the data points that can be predicted using the 3 constant motor model. This analysis begins with equation {16} derived using Kirchhoff's law.

$$E_i = E - IR_m \quad \{16\}$$

Equation {16}, along with the 3 motor constants, can be used to find the stall current (I_{stall}) and no load speed ($RPM_{no-load}$). The stall current ($Eq.\{17\}$) occurs when the motor is stopped; this means that there is no back-EMF voltage generated in the motor.

$$When\ I = I_{stall}\ , E_i = 0\ .\ Therefore,\ I_{stall} = \frac{E}{R_m} \quad \{17\}$$

To find the no-load speed, we can use the no-load current (I_0), the back-EMF constant (K_v), and equation {18}. The no-load current (I_0) and back-EMF constant (K_v) are fundamental motor constants and must be measured. First, using the no-load constant and equation {16}, we can get the back-EMF (E_i) voltage generated by the motor. Next, we use the back-EMF (kV) constant to find the no load RPM of the motor.

$$E_{i,no-load} = E - I_{no-load}R_m\ ,\ RPM_{no-load} = kV * E_{i,no-load} \quad \{18\}$$

With some manipulation of the 3 constant model equations, the max efficiency can be calculated using equation {19}. Similarly, the maximum power can be calculated using equation {20} [35].

$$\eta_{max} = \left(1 - \sqrt{\frac{I_0 R_m}{E_i}}\right)^2\ ,\ P_{max} = \frac{E^2 - (R_m I_0)^2}{4R_m} \quad \{19\}\ ,\ \{20\}$$

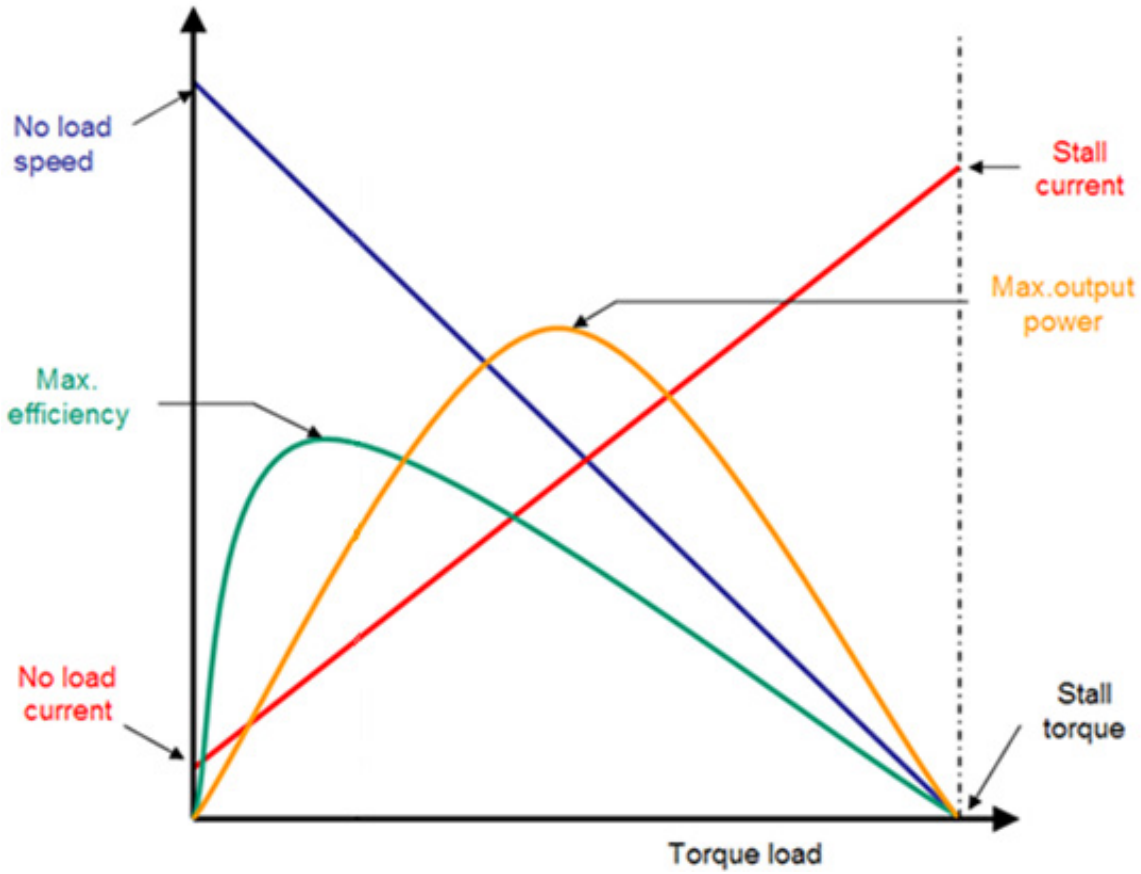

Figure 13. Motor Curve of Ideal BLDC Motor

The final point of interest is the stall torque (τ_{stall}) of the motor. This point can be found using the torque constant of the motor (K_t). K_t is dependent on the back-EMF constant by equation {21}. This equation shows the inverse relationship between input power and opposing back-EMF voltage discussed earlier. With K_t and the stall current (I_{stall}), the stall torque is calculated with equation {22}.

$$K_t = \frac{60}{2\pi * K_v} \ , \ \tau_{stall} = K_t I_{stall} \qquad \{21\} \ , \ \{22\}$$

While the theoretical framework is sound, discrepancies arise when the theoretical motor predictions are compared with experimental data. Figure 14 shows a sample motor's theoretical and experimental torque curves. The majority of the error originates

from the calculation of the stall torque. This error could be caused by erroneous motor constants (either in measurements or supplied by manufacturer), imperfections in the motor (such as sloppy windings, delaminated layers, or overheated magnets), or losses not accounted by the 3 constant model (eddy currents or external damping effects). Whatever the case may be, it is clear that the 3 constant motor model can't be utilized to the same degree as the BEM theory model [29].

Thus, due to the errors in the motor modelling, it was decided only the experimental data could be trusted for further calculations. The data was gathered using the motor test bed as discussed in the experimental section. Experimental data is shown in Figure 14 as well. It confirms that the behavior of the real BLDC motor is much different that the idealized case.

4.2. Combining Motor Curves and Propeller Theory

Finally, to calculate the operational point of a motor and propeller pair, the data from BEM theory and the experimental motor data is combined using a RPM-Torque curve as shown in Figure 15. The intersection point (highlighted in red) represents the point at which this particular motor and propeller combination will operate. With this operational point, the total thrust, current, motor efficiency, and power can be found using the other motor and propeller curves.

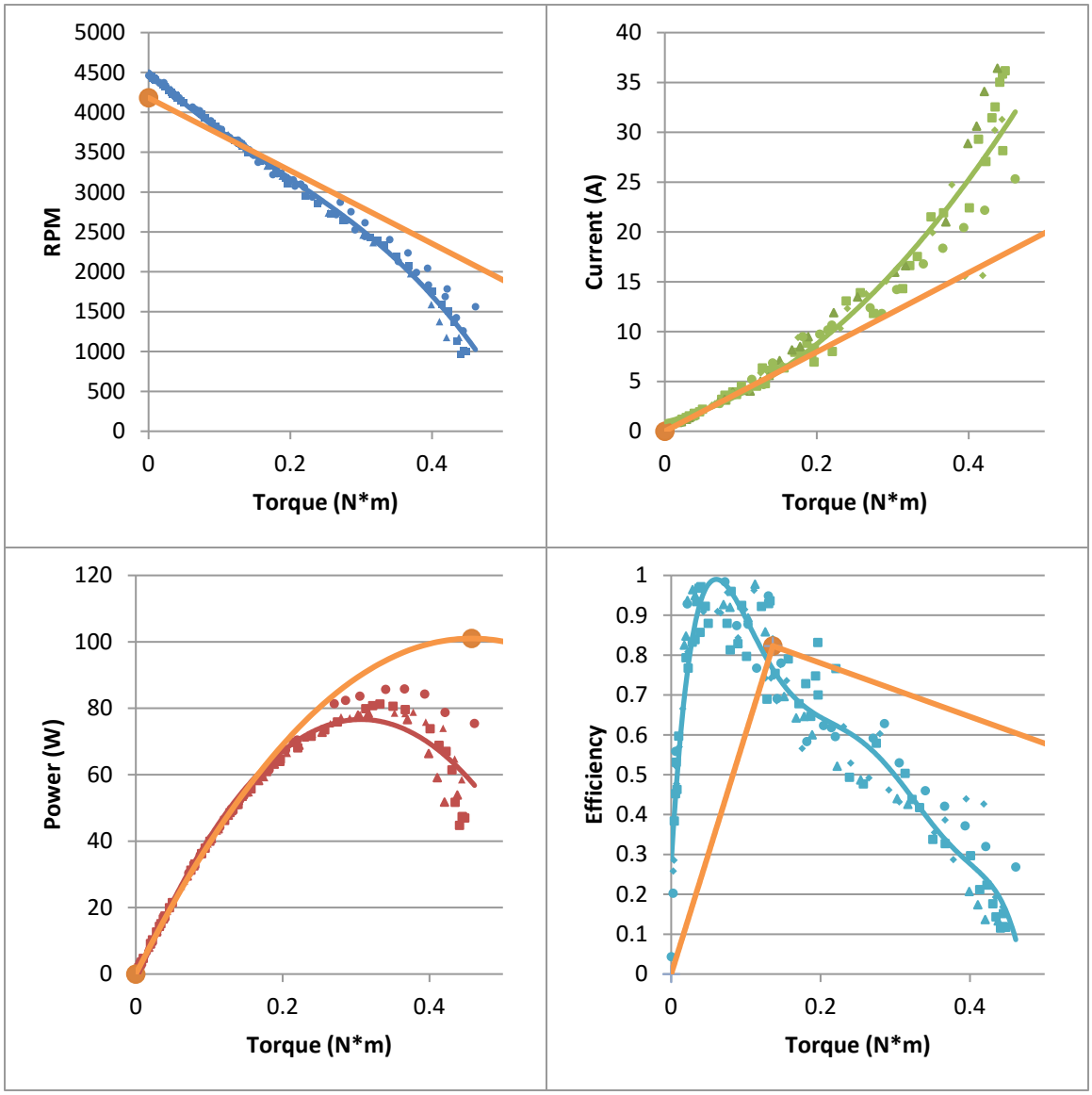

Figure 14. 380Kv Theoretical and Experimental Motor Curve Comparison

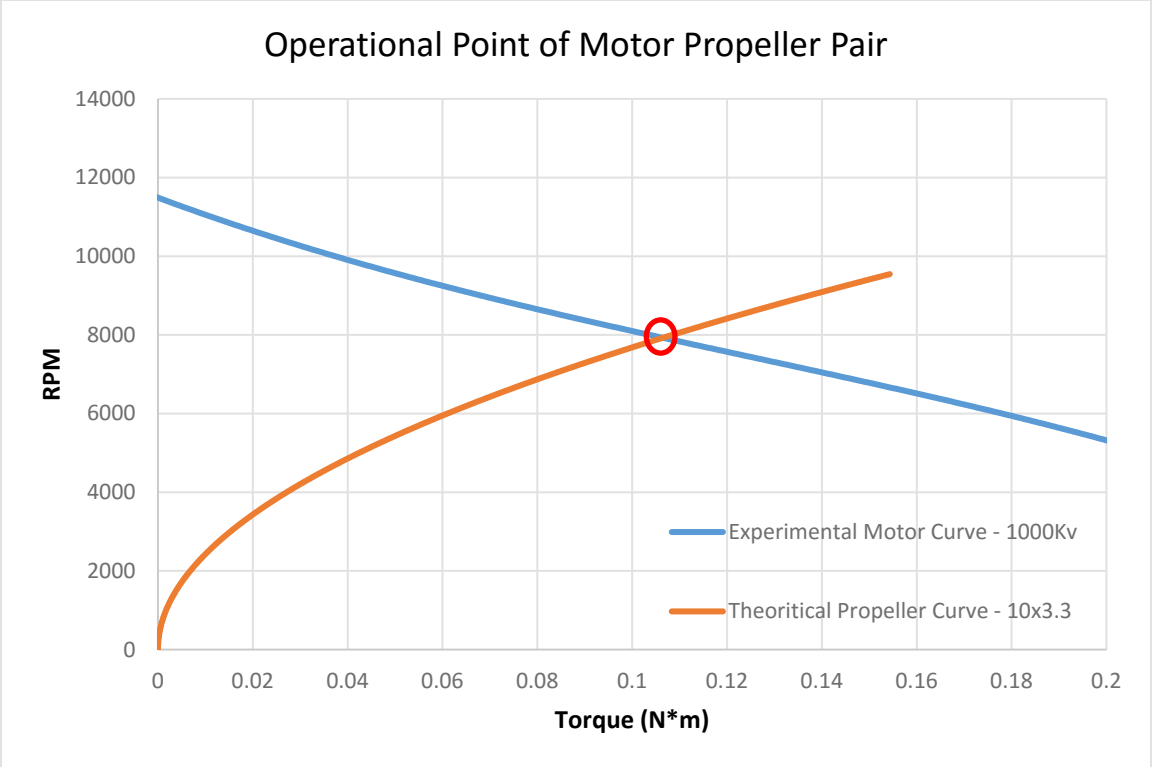

Figure 15. Operational Point of Motor Propeller Pair

4.3. Manufacturer Data Comparison

Most reputable motor manufacturers supply motor performance data for several propeller sizes to help customers select the proper power system for their application. After some preliminary motor and propeller performance data was collected using the aquarium tank test bed, some discrepancies were noted in the g/W efficiencies reported by manufacturers and experimental data. This called the validity of the experiment into question and needed to be investigated to root out any unknown parasitic losses. In addition, any available manufacturer data is usually consulted during procurement decisions and if the data is inaccurate, it should be noted during future design consultations.

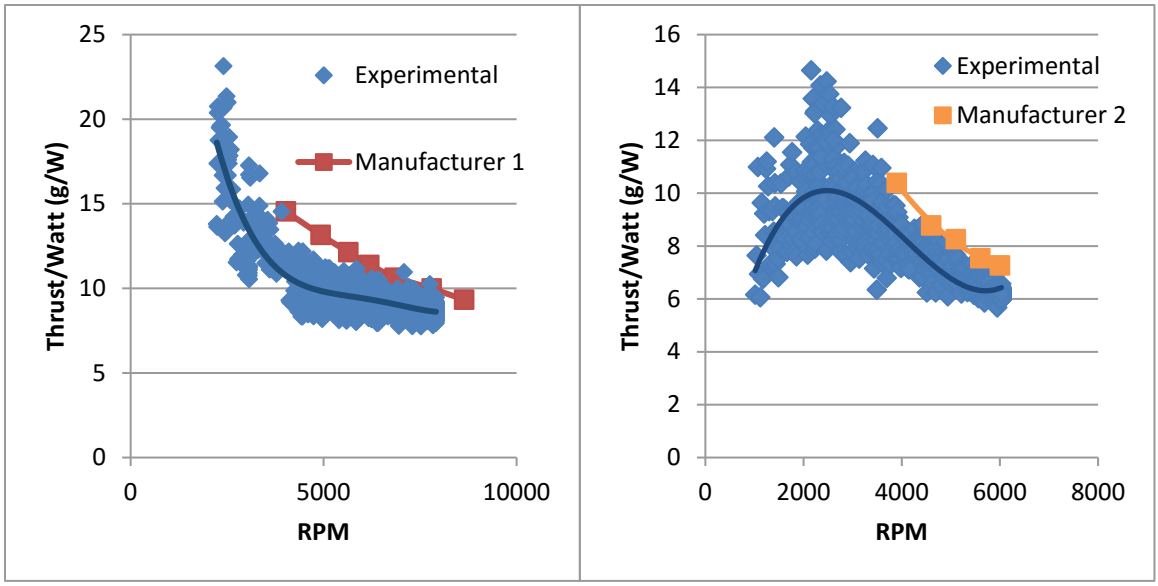

Figure 16. Comparison between Manufacturer and Experimental Data for two Different Mfg., Motors, Propellers, and ESCs

Using the manufacturer recommended motor, propeller, and ESC components, data was gathered on the tank test bed and empty water tunnel test bed. After multiple tests with recommended setups from 2 leading manufactures, who shall remain nameless, a trend emerged in the data as seen in Figure 16. The manufacturer supplied data for both tests aligns with upper edge of experimental data for both companies. Upon closer inspection, it is observed the discrepancies are focused in the reported current values between the manufacturer and experimental data. In the experimental setup, a calibrated current and voltage sensor and a calibrated DC power supply are used to rule out any offset errors. This implies that manufacturers cherry-pick their best data points and customers should be wary when designing based on said data. Since current is usually not measured in most multirotors, this discrepancy may be difficult to observe in normal power systems. This data suggests that while manufacturer reported performance is possible in the optimal conditions, the average system performance will be significantly lower than these data points.

4.4. Propeller Experiments and Results

Previous studies have proven that ESCs are extremely efficient with data suggesting near 95% efficiency over most of their operational range [31]. Therefore, the other components in the power system must be examined to determine their effectiveness in a submersible UAV. Work has been done in several studies to build a comprehensive database for RC air propeller performance data [33]. While no propeller manufacturers provide the exact shape of their airfoils, matching the diameter and pitch is sufficient for rough comparison of propellers from different manufacturers. Using equations, the same methods used to calculate propulsive efficiency in air can also be used in the water tunnel.

$$\eta_{Prop} = \frac{T * U_\infty}{P_{in}}\ , \qquad where\ T\ is\ the\ thrust, U_\infty\ is\ the\ flow\ velocity\ in\ the\ tunnel,$$

$$and\ P_{in}\ is\ the\ input\ power\ to\ the\ propeller\ (same\ as\ the\ output\ power\ of\ the\ motor)$$

$$P_{in} = P_{motor} = 2\pi nQ\ ,$$

$$where\ n\ is\ revolutions\ per\ second, and\ Q\ is\ the\ torque \qquad \{23\}\ ,\ \{24\}$$

These calculations, plotted in Figure 17, show the RC propeller efficiency in air and water. While the LEFTE lab water tunnel is unable to collect data over the entire curve due to flow speed limitations, the partial curve shows that an RC propeller is efficient in water. This data strongly supports the plausibility of using RC air propellers in air and water. Other experiments were also conducted using different motors paired with the same propeller. This data, also shown in Figure 17, reproduces the same efficiency curve verifying the efficiency of the propeller in water. This data is compared

to a similarly sized propeller in air in Figure 17 which confirms the efficient behavior of the propeller in air and water.

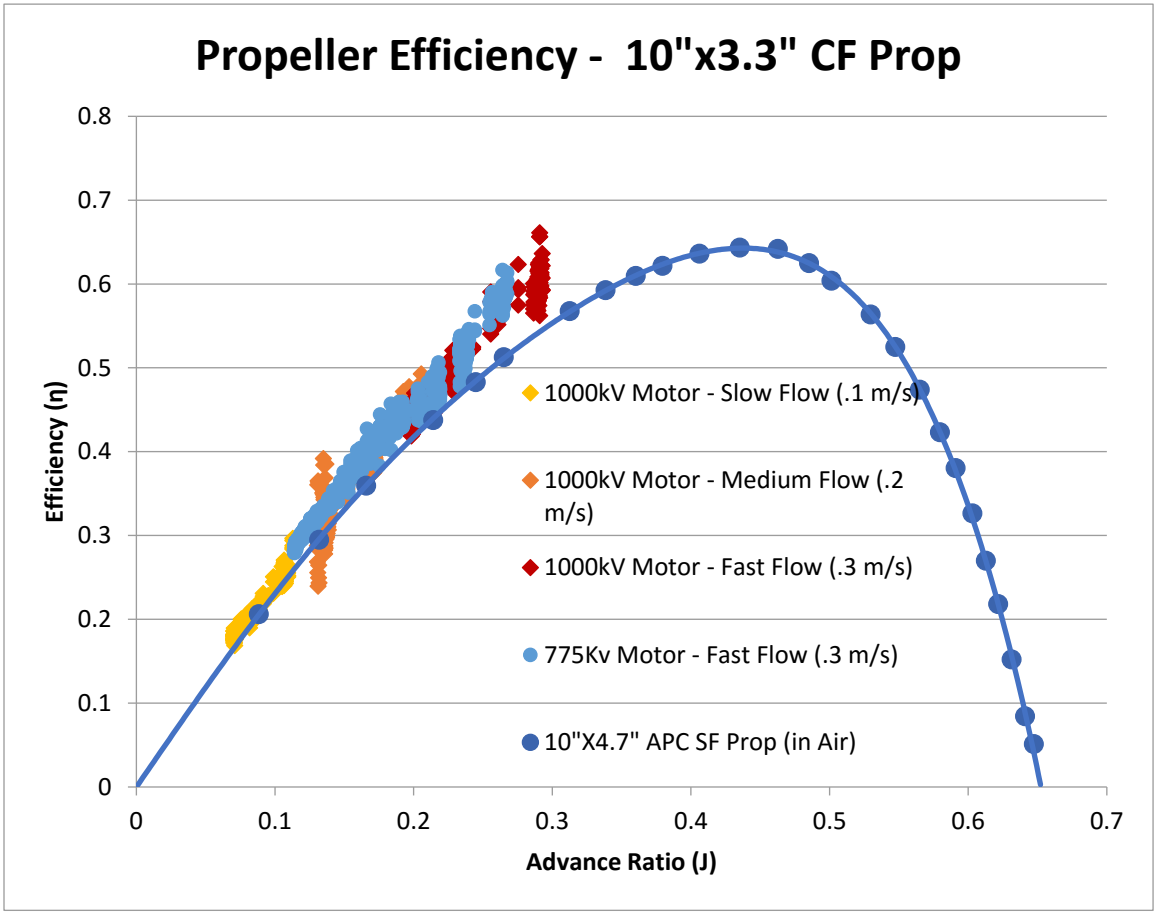

Figure 17. Propeller Efficiency in Air and Water

4.5. Motor Experiments & Results

The last component in the system is the BLDC motor that transforms electrical energy into mechanical energy. Motor performance is usually presented using characteristic torque curves. These curves present the RPM, current, power, and efficiency as a function of the torque. Figure 13 shows the standard motor curve of an ideal BLDC motor with important points highlighted of each curve. The standard technique of plotting these curves is to measure the RPM and current of the motor with

no load, and current and torque at motor stall. Then, a linear approximation is used between these two points and the power and efficiency curves are calculated using equations {24} and {25}.

$$\eta_{motor} = \frac{2\pi nQ}{VI} \quad \{25\}$$

However, a problem arises when this technique is used with BLDC motors. Creating a motor stall in a BLDC motor is a serious concern due to 2 factors; the high discharge capability of Li-Po batteries and the low resistance of a brushless motor. While in normal operation a generic BLDC motor may consume on the order of 20 amps, during stall, the same motor may draw over 300 amps through it. This is exacerbated by the fact that most well-made Lithium polymer batteries are capable of discharging such high current. This current generates enormous heat in the motor causing the magnet wire inside the motor to de-laminate in a matter of seconds and burn out the motor. This much current would also destroy almost any motor controller. To prevent this catastrophic failure, modern ESCs have stall detection circuits that detect extreme currents and reset the commutation of the motor. This causes the motor to jitter back and forth when stalled protecting the components, but also making measurement of the stall torque impossible.

This problem can be circumvented using the motor test bed. This testbed acts as a Prony brake dynamometer that would measure the torque while the motor is still rotating [36]. This test bed was used to create experimental curves such as in Figure 18 and easily compare the performance of many different motors.

The torque testing was also conducted underwater to ascertain the effect on the motor curves. These tests are also presented in Figure 18. As seen in this figure, the water

causes to motor to idle at a lower RPM and higher current than when in air. This is due to the increased skin drag of the water on the motor. Besides that, there are no other performance differences between the mediums. This shows that motors that will operate in water don't have to be tested in water as well; the motor curves measured in air will remain constant between the mediums.

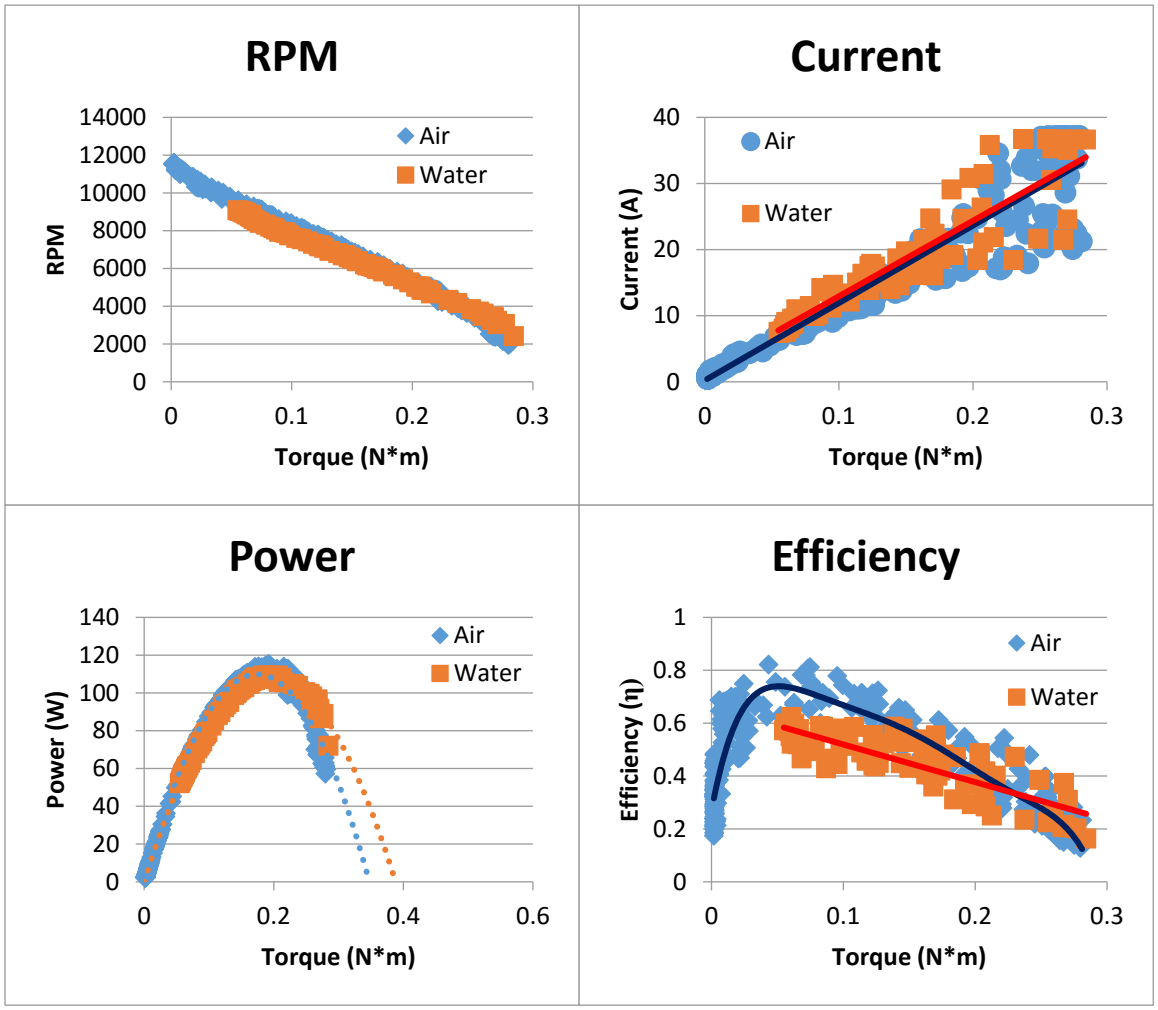

Figure 18. Motor Torque Curves in Air and Water

4.6. Voltage Testing

The battery of a multirotor is usually the heaviest component of the system. A standard lithium-polymer pouch cell generates a nominal voltage of 3.7 volts. Cells are added in series to increase the voltage of the pack and cells in parallel increase pack capacity. Since a high voltage battery pack significantly increases weight but contributes nothing to battery capacity, the benefit of using high voltage packs versus a low voltage, high capacity was questioned. To that end, an examination of the effects of battery voltage on motor performance was conducted.

A NTM 1000Kv motor, with a manufacturer recommended operating voltage of 12V, was used as the control motor for this experiment. Motor curves were collected at step voltages which correspond to Li-Po batteries of 2s(8V), 3s(12V), and 4s(16V) packs and plotted in Figure 19. This data shows BLDC motors operate more efficiently at higher voltages. This finding makes sense because for a given output wattage of the system, using a higher voltage will reduce the current flowing into the motor[P=IV]. Power losses are quadratically related to current [$P_{loss} = I^2R$] so reducing the current will always reduce losses and make the system more efficient. Another finding from these motor curves was that as the applied voltage was increased, the maximum current drawn by the motor also increased. This means that at the higher voltage, the motor is also able to develop more overall power at an increased efficiency.

Normal Li-Po batteries are made of discrete, equally sized pouches; the energy density remains the same no matter what configuration the battery takes. For two battery packs with the same number of cells, one with high voltage & low capacity, and another

with low voltage & high capacity, the high voltage battery will provide higher endurance due to the reduction in wasted energy as resistive heating. Therefore, by using higher voltage battery packs, resistive losses are reduced and higher performance capabilities are available. Thus, this data supports the use of higher voltage batteries in a multirotor system.

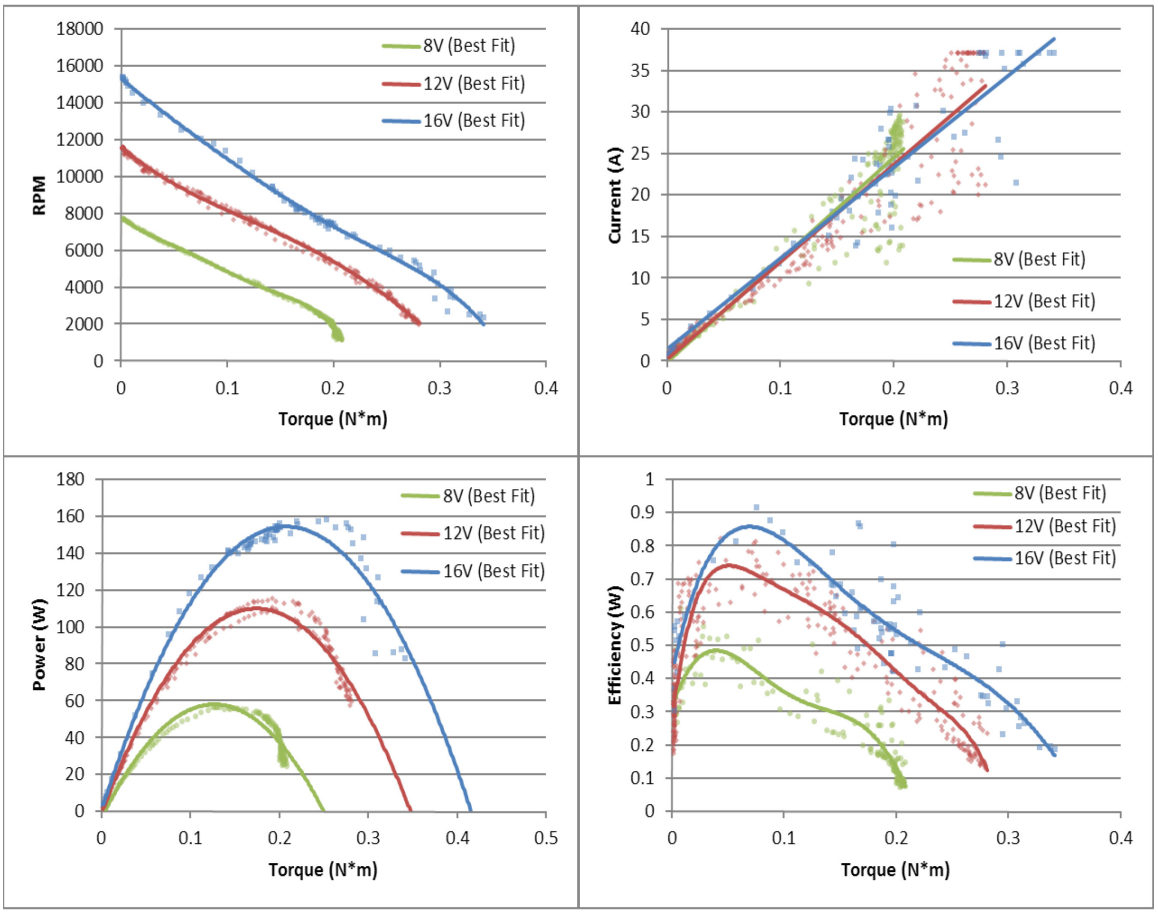

Figure 19. Torque Curves of NTM 1000Kv Motor at Various Voltages

4.7. Throttle Testing

The next parameter to determine is the agility of a multirotor vehicle. In mathematical terms, agility is usually defined by the thrust-to-weight ratio of a multirotors. For example, heavily loaded copters burdened with cameras and batteries may have a minimal T-W ratio of 1.2:1 which leads to slow, unwieldly maneuvers. On the other hand, FPV racing quadcopters can have an extreme T-W ratio of 13:1 for acrobatic maneuvers and aggressive flying. Most multirotor flight controller manufacturers recommend having a T-W ratio of 2:1; such a T-W ratio would allow the vehicle to hover at 50% throttle and maintain good maneuverability and control.

As mentioned in the introduction, multirotors achieve control by varying the RPM of individual motors. This is the crucial foundation upon which the multirotor control scheme is built. Multirotor throttle variation is done by Pulse Width Modulation (PWM) in the ESCs. The ESC uses high frequency MOSFETs to rapidly pulse on and off to control the average voltage applied to the motor. This means that when a normal quadcopter is hovering at 50%, the effective voltage applied is only half of what the recommended voltage of the motor. Voltage testing has shown that efficiency decreases with voltage so PWM control may also be decreasing the efficiency. In that case, it would be beneficial to sacrifice some agility with a low T-W ratio in favor of increased efficiency and endurance.

To test the effects of PWM control on motor curves, experiments at different throttle levels were conducted on a new NTM 1000Kv motor. The motor was tested at 3s(12V) voltage per manufacturer recommended specifications and the motor curves are

plotted in Figure 20. These curves show that PWM control works very well at controlling RPM in a BLDC motor. The RPM-torque curves are smooth and parallel indicating a constant gradient according to the effective voltage applied to the motor. The sharp drops at the beginning of the partial throttle RPM-torque curves are caused by the nature of PWM control. This modulation technique works on pulsing the motor with bursts of either full power and no power. With this method, it takes substantially more power to accelerate the motor which stresses the FET switches in the ESC. Thus, the ESC software is designed such that at partial throttles, the motor always runs at a high speed and when a load is applied, it decelerates to the correct function curves. Fortunately, these drops don't impede the effectiveness of the motor because, as shown in Figure 15, the operational points of a motor with a propeller generally don't occur near these areas. PWM control does incur about 10% efficiency loss (Figure 20) as compared to without it over the whole throttle spectrum. However, since the loss is minimal, designing and operating a multirotor motor at a 2:1 T-W ratio should be acceptable given the additional gains in maneuverability.

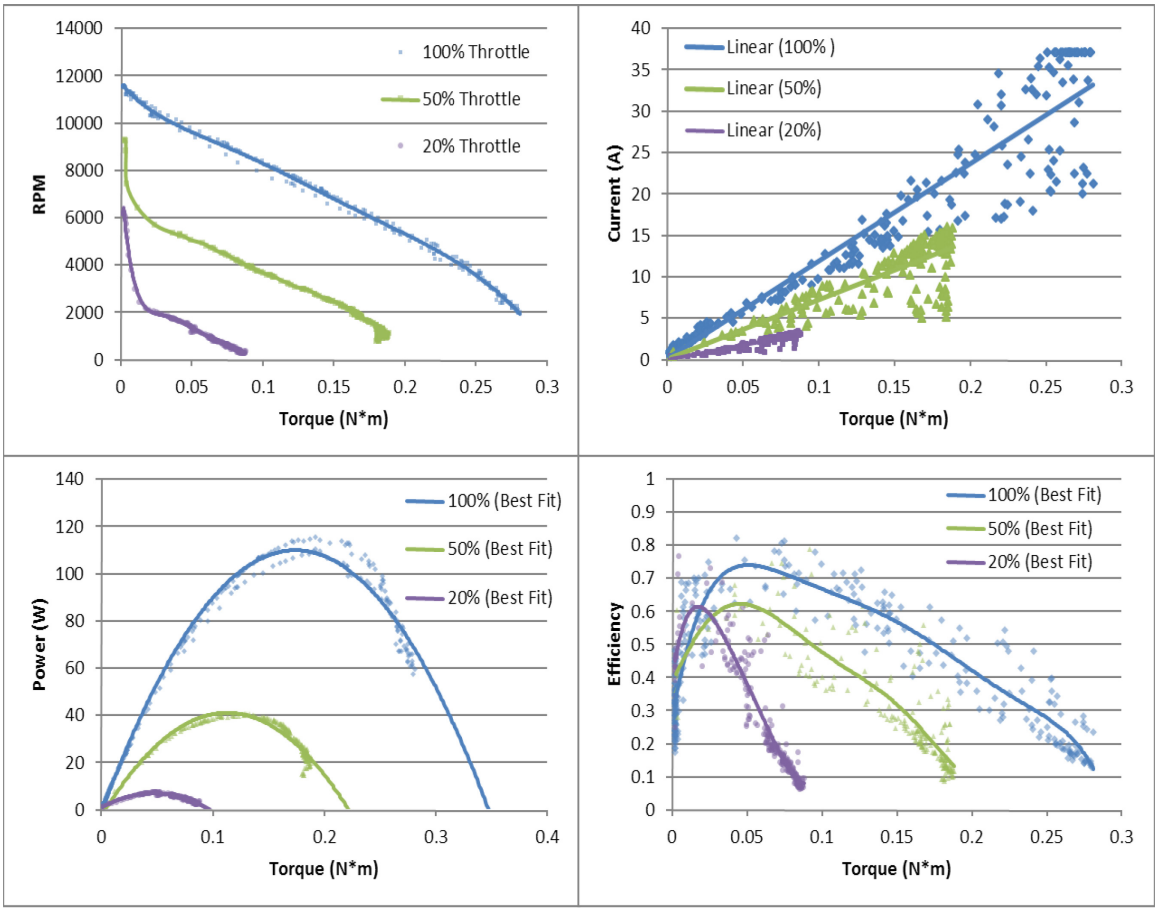

Figure 20. Torque Curves of NTM 1000Kv Motor at Various Throttles

4.8. Corrosion Testing

Corrosion protection testing was a practical requirement that was discovered during testing of earlier motors in water. Motors that had prolonged exposure to water exhibited rusting and made grinding sounds due to lubrication being washed away from the bearings. To protect these components in the future, anti-corrosion compounds were sprayed on the motors and tested for longevity and adverse performance degradations. Motors coated with WD-40, CorrosionX, and CorrosionX HD were tested in the tank test bed. One motor coated with each compound and a control motor were left in agitated water for 24 hours. After drying, each was taken apart and visually inspected. No

corrosion was observed on any of the coated motors. The plain motor showed some signs of corrosion on the stator teeth and made grinding sounds when rotated.

Next, 3 new motors were coated with each of the coating compounds and tested in the tank test bed. Of the 3 coated motors, only the motor coated with CorrosionX HD showed some performance reduction. CorrosionX HD is the most viscous of all three coatings but the performance drop is very slight as shown in Figure 21. After this testing, it was recommended to coat all future motors with CorrosionX (regular version). This was recommended because unlike, WD 40, it is lubricant as well as corrosion inhibiter which can protect the stator and lubricate the bearings. Independent testing has also shown that it provides as much corrosion protection as WD 40 [37].

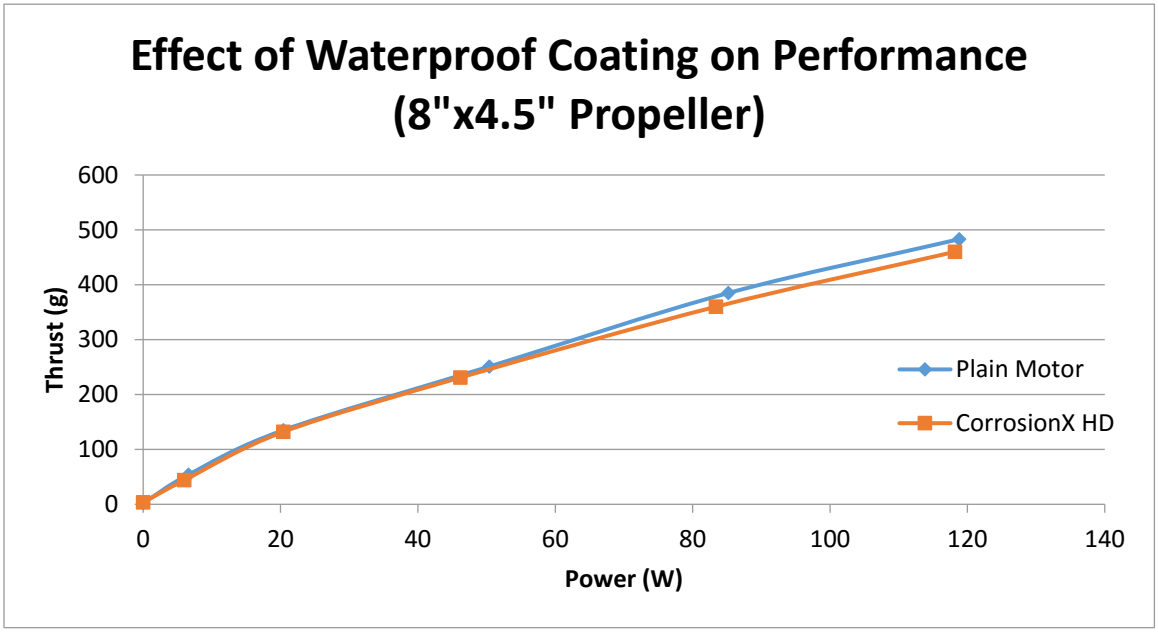

Figure 21. Performance Effects of CorrosionX HD on NTM 1000 Kv Motor with 8x4.5 Propeller

4.9. Case Study - Naviator V5 Prototype

All the concepts, theoretical predictions, and experimental data of the previous sections were used to design the power system for the Naviator submersible-UAV [38]. This case study can be found in the appendix.

5. Conclusion

This report presented a realistic approach for modeling UAV motors and propellers for use in air and water. Three test beds were constructed to validate the theoretical models and collect data. Data was taken to observe the effects of torque, thrust, voltage, current, speed, propeller and motor size. It was found that a realistic BEM theory model could be constructed that can predict the behavior of RC propellers with a high degree of accuracy. This data was verified using 2 different test beds and multiple propeller trials. Unfortunately, a sound 3 constant motor model could not match the accuracy produced by the BEM theory model. This is likely due to high sensitivity of the motor models to measurement errors. This setback was bypassed by directly measuring the motor curves using the motor test bed. The theoretical propeller data and experimental motor data was combined to produce operational points for any motor-propeller combination of the tested components.

Further experiments were carried out to determine behavioral characteristics of UAV power system components in air and water. These tests showed that an RC air propeller is equally efficient in air and water, and the behavior of a BLDC motor does not generally vary between the two mediums. Other tests showed that a BLDC motor is more efficient at higher voltages and is maintains its efficiency throughout its operational throttle range. This corroborates other sources which state that an ESC is highly efficient (>95%) over its operational throttle range.

Conclusions from this research was incorporated into a case study to design the power system of the Naviator submersible-UAV multirotor prototype. With specifications for the weight, agility, and endurance of the vehicle, a parts selection for

the motor, propeller, ESC, and battery was recommended using logical conclusions from system constraints and available research data. The capability of the recommended components was tested and confirmed to be functioning within the design specifications. Some practical considerations were also incorporated in the design recommendations to increase endurance and longevity.

The data presented in this thesis can be used for future designs of a multi-medium multirotor and drones in general. With the rapid expansion of the professional UAV industry and the diverse drone projects being built by RC enthusiasts, a deeper understanding of the UAV power system is a crucial first step to any successful drone project.

Bibliography

[1] W. R. Young, The Helicopters (Epic of Flight), Chicago: Time-Life Books, 1982.

[2] The Royal Aero Club, "A Successful French Helicopter," *Flight - The Aircraft, Engineer, & Airships,* p. 47, 24 1 1924.

[3] "Levitation - Translation," *Flight,* p. 696, 12 11 1954.

[4] G. Apostolo, The Illustrated Encyclopedia of Helicopters, New York: Bonanza Books, 1984.

[5] C. Jefford, The RAF Harrier Story, London: Royal Air Force Historical Society, 2006.

[6] Draganfly Innovations Inc., "The story behind Draganfly Innovations," 2016. [Online]. Available: http://www.draganfly.com/our-story/. [Accessed 2016].

[7] DJI, "Inspire 1," 2016. [Online]. Available: http://www.dji.com/product/inspire-1.

[8] A. Fabio, "Droning On: Choosing a Flight Controller," HackADay, 2014. [Online]. Available: http://hackaday.com/2014/06/06/droning-on-flight-controller-round-up/. [Accessed 2016].

[9] F. Pasolini, "MEMS Accelerometers, Gyroscopes, and Geomagnetic Sensors - Propelling Disruptive Consumer Applications," Digi-Key, 2011. [Online]. Available: http://www.digikey.com/en/articles/techzone/2011/apr/mems-accelerometers-gyroscopes-and-geomagnetic-sensors---propelling-disruptive-consumer-applications. [Accessed 2016].

[10] C. Mathas, "Sensor Fusion: The Basics," Digi-Key, 2012. [Online]. Available: http://www.digikey.com/en/articles/techzone/2012/apr/sensor-fusion-the-basics. [Accessed 2016].

[11] A. Gibiansky, "Quadcopter Dynamics, Simulation, and Control," 2010. [Online]. Available: https://www.researchgate.net/file.PostFileLoader.html?id=560c1e485f7f7136b78b45fc&assetKey=AS%3A279438592888842%401443634760742. [Accessed 2016].

[12] a. C. A. B. Kunzmann Juergen, "Investigations in the control of a four-rotor aerial robot," in *Proceedings of the 2nd IASTED International Conference on Robotics (ROBO 2011)*, Pittsburgh, 2011.

[13] P. J. McKerrow, "Modelling the Draganflyer four-rotor helicopter," in *Robotics and Automation Vol.4, pg. 3596 - 3601*, New Orleans, 2004.

[14] NRC Reseach Press, "Journal of Unmanned Vehicle Systems," Canadian Science Publishing, 2014. [Online]. Available: http://www.nrcresearchpress.com/journal/juvs. [Accessed 2016].

[15] Sinclair National UAS Training & Certification Center, "Journal of Unmanned Aerial Systems," NRC Research Press, 2013. [Online]. Available: http://uasjournal.org/. [Accessed 2016].

[16] S. M. Hogan, The Drone Revolution: How Robotic Aviation Will Change the World, Tallahassee, Florida: CreateSpace Independent Publishing Platform , 2015.

[17] Midwest Research Institute, "BRUSHLESS DC MOTORS," N.A.S.A, Kansas City, 1975.

[18] K. S. D.J. Auld, Aerodynamics for Students, Sydney: The University of Syndey, 2006.

[19] M. S. S. John B. Brandt, "Propeller Performance Data at Low Reynolds Numbers," in *49th AIAA Aerospace Sciences Meeting*, Orlando, 2011.

[20] "Engineering Design Process Used to Develop APC Propellers," APC Propellers, 2015. [Online]. Available: https://www.apcprop.com/Articles.asp?ID=262. [Accessed 2015].

[21] H. Y. Mark Drela, "XFOIL Subsonic Airfoil Development System - NACA 4412 Xfoil prediction," 2013. [Online]. Available: http://airfoiltools.com/polar/details?polar=xf-naca4412-il-50000. [Accessed 2015].

[22] J. G. Leishman, Principles of Helicopter Aerodynamics, New York: Cambridge University Press, 2006.

[23] C. R. Harman, "PROPX: Definitions, Derivations, and Data Flow," Oregan State University, Corvallis, 1994.

[24] Ron/spinningmagnets, "Motor tech: Learn the Terms," 14 05 2014. [Online]. Available: https://www.electricbike.com/motor-tech-learn-the-terms-part-1/. [Accessed 2016].

[25] R. Büchi, Brushless Motors and Controllers, Books On Demand, 2012.

[26] *Brushless DC Motors & Control - How it Works.* [Film]. U.S.: Texas Instruments, 2012.

[27] U. D. o. Energy, "Department of Energy Fundamentals Handbook: Electrical Science Module 5 - DC Generators," Integrated Publishing , Washington, D.C. , 1992.

[28] S. Keeping, "Controlling Sensorless, BLDC Motors via Back EMF," Digi-Key, 2013. [Online]. Available: http://www.digikey.com/en/articles/techzone/2013/jun/controlling-sensorless-bldc-motors-via-back-emf. [Accessed 2016].

[29] J. Carri, "A four-constant model for electric motors," 2007. [Online]. Available: http://flbeagle.rchomepage.com/research/4_consts_paper_ver_02.pdf. [Accessed 2016].

[30] J. M. F. d. P. Darren Lance Gabriel, "Brushless DC Motor Characterisation and Selection," in *IEEE Africon 2011*, Livingstone, Zambia, 2011.

[31] R. A. M. Clayton R. Green, "Modeling and Test of the Efficiency of Electronic Speed Controllers for Brushless DC Motors," in *15th AIAA Aviation Technology, Integration, and Operations Conference*, Dallas, 2015.

[32] Sensing Systems, "Underwater Torque Sensors / Submersible Torque Sensors," Sensing Systems Corp., [Online]. Available: http://www.sensing-systems.com/underwater-torque-sensors. [Accessed 2016].

[33] J. B. Brandt, "UIUC Propeller Database - Volume 1," 2015. [Online]. Available: http://m-selig.ae.illinois.edu/props/volume-1/propDB-volume-1.html. [Accessed 2016].

[34] A. Rohatgi, "WebPlotDigitizer," 2015. [Online]. Available: http://arohatgi.info/WebPlotDigitizer/app/. [Accessed 2016].

[35] J. Bergmeyer, "Feature Article - Motor Constants, How To Find Them And Use Them," RCGroups, 2003. [Online]. Available: http://www.rcgroups.com/forums/showthread.php?t=185271. [Accessed 2016].

[36] B. E. Babcock, "The Design, Construction, and Use of a SMALL PRONY BRAKE," *Gas Engine Magazine,* 7 2000.

[37] "Comprehensive Corrosion Test: 46 Products Compared," Day At The Range, [Online]. Available: www.dayattherange.com/?page_id=3667. [Accessed 2016].

[38] P. V. S. F. J. D. Marco M. Maia, "Demonstration of an Aerial and Submersible Vehicle Capable of Flight and Underwater Navigation with Seamless Air-Water Transition," *arXiv preprint,* no. arXiv:1507.01932, 2015.

6. Appendix

6.1. Case Study - Naviator V5 Prototype

All the concepts, theoretical predictions, and experimental data of the previous sections were used to design the power system for the Naviator submersible-UAV [38]. This system consisted of the 4 components; the battery, ESC, motor, and propeller. Some design constraints were placed on each component. First, the components must be commercially sold to expedite prototype construction. While custom components could be tailored to better suit this application, prefabricated parts offer consistent, reliable performance at an affordable cost. Next, it was recommended to use Li-Po batteries as the power source for the prototype due to their high energy density, high discharge rates, low cost, and broad availability in many sizes. Third, the ESC selection was reduced to the Flycolor 3s-8s 45A ESC because it was the only controller able to provide consistent and reliable performance in air and water. Finally, propeller materials were limited to carbon fiber only due to its superior rigidity and strength.

The vehicle's All-Up Weight (AUW) was specified at 6 kg (dry vehicle, battery, sensors) with a minimum flight time of 30 minutes in air. To maintain its ability to transition from air and water, the multirotor was configured to be X-8. This meant the thrust would be distributed over 8 motors and propellers. This prototype was designed as a platform to develop underwater sensor nodes, control algorithms, and ground communications modules. As such, it will be subject to indoor testing where control must be maintained at all times to prevent injuries to bystanders. Thus, it was also specified that the vehicle has good agility by maintaining a Thrust-to-Weight (T/W) ratio of 2:1.

The motor voltage analysis from earlier sections show that operating at a higher voltage is more efficient for a BLDC motor. With the controller fixed to the Flycolor 3s-8s ESC, the highest available voltage is 30V (8s). However, during some preliminary trials with test motors, it was found that this ESC also exhibited some unstable behavior at 30V underwater. Thus, the operating voltage was reduced to the next standard Li-Po size of 22.2V (6s). The capacity of the battery will be determined after motor selection.

Earlier comparisons between experimental and manufacturer data has shown inaccuracies in the manufacturer provided data. Unfortunately, short of buying and testing hundreds of sample motors, this data is the only available source of information and must be consulted. To compensate for the inaccuracies, a 30% safety factor was added to all requirements. Next, using the AUW, T/W ratio, and safety factor, the maximum required thrust is calculated to be 1900g per motor. With this thrust requirement and the battery voltage, the motor choices were narrowed to 7 motors. One of each sample motors were purchased and tested on the motor test bed to determine its motor curves. Their sizes ranged from 28mm to 40 mm, and their Kv ranged from 270Kv to 775Kv. Then, using BEM theory, the thrust and torque curves of propellers ranging from 10” to 18” were calculated. Each motor and propeller combination was tried to find one that could provide the required thrust with the lowest power consumption.

The final combination was selected as the MN 4014 330 Kv motor, and 15”x5” CF propeller. These components fulfilled the requirements perfectly, and the motor was slightly oversized for this application. This allowed for larger propellers to be used in the future should the AUW increase from additional payloads. With the motor, propeller, ESC and battery voltage determined, experiments with these components were carried out in the tunnel test bed. The air tests, shown in Figure 22, confirm that these

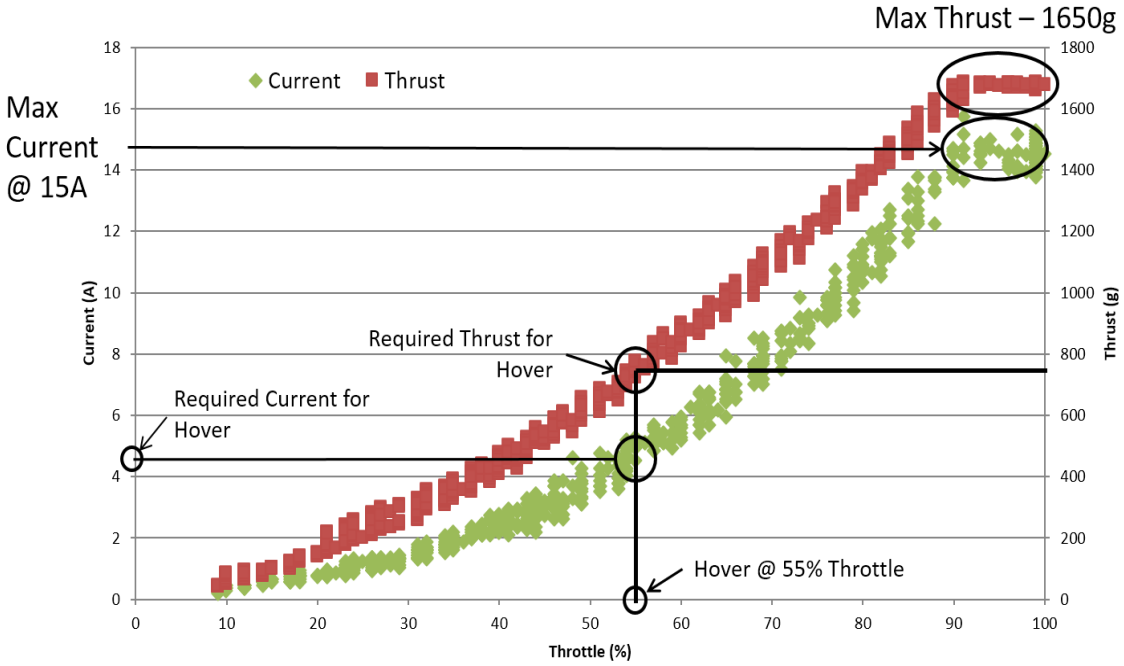

Figure 22. Performance of 330Kv Motor and 15x5 Propeller

components produce thrust and power at predicated values. The water test, shown in Figure 23, show good performance in water as well. Of particular note is the very low RPM of the propeller in water and the very high thrust output. Compared to the air performance, for about twice the input current, this motor-propeller combination produces quadruple the thrust in water. Using Figure 22 and the AUW of the vehicle, the required battery size can now be calculated.

A multirotor in flight consumes the least power when it is in hover. As opposed to lateral flight, the hover state only produces enough thrust to equal the vehicle weight.

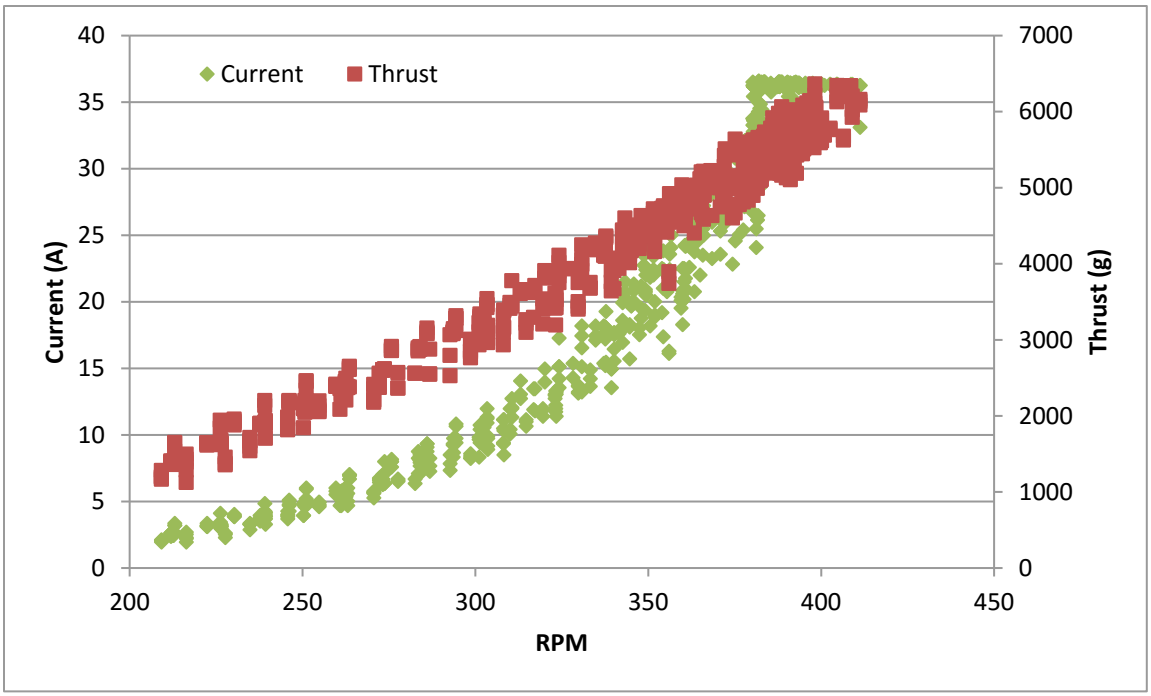

Figure 23. Performance of Naviator Power System in Water

Therefore, a multirotor's maximum endurance is when it is hovering. The current consumption during hover can be calculated using Figure 22. Then, equation {26} can be used to calculate the required capacity for a flight time of 30 minutes. Battery manufacturers also recommend a safety factor of 1.3 to make allowances for external factors which can affect battery life.

$$Endurance = \frac{Capacity}{Consumption * 8 * S.F.}\ ,\ where\ capacity\ is\ in\ Amp-hours,$$

$$and\ consumption\ is\ in\ Amps\ (x8\ for\ 8\ motors) \qquad \{26\}$$

From this calculation, the minimum required battery size is 24,000 mAh for a flight time of 30 minutes. From this result, a good choice would be the Turnigy 8000mAh 6S 25C Li-Po battery with 3 packs in parallel. However, this is a high discharge battery

that can continuously output ~600A. From the experimental results in Figure 22, we know that the maximum possible current consumption of this prototype is only ~150A. A better choice would be the Multistar High Capacity 6S 10C 10000mAh battery with 3 packs in parallel. This lower discharge configuration weighs the same, is capable of supplying the required current, and has a flight time of 38 minutes.

6.2. *Kv* Comparision

Figure 24 shows the RPM-Torque curve of four similarly sized motors with different *Kv* ratings. These experiments were done with an applied voltage of 12 V to all motors. As seen in Figure 24, motors with higher Kv ratings are higher up on the RPM axis. It is interesting that all of the curves are seem mostly parallel with each other. This is due to the fact that lower kV motors are not optimized to run at low voltages. Even though all these motors are similarly sized, the manufacturer recommended voltage for the lower Kv motors (380Kv ,268Kv) is more than double the recommended voltage of the higher Kv motors (740Kv, 775Kv). Figure 25 shows the RPM torque curve of the low Kv motors at

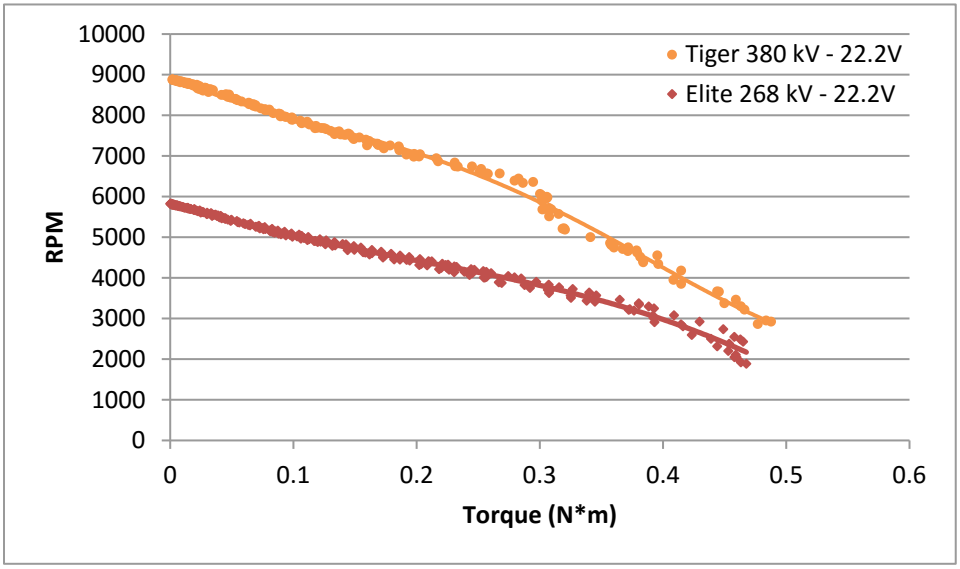

Figure 25. Low Kv Motors at Recommended Operating Voltages

more optimized voltages. Since these datasets are at different voltages, the motors cannot be directly compared to each other anymore.

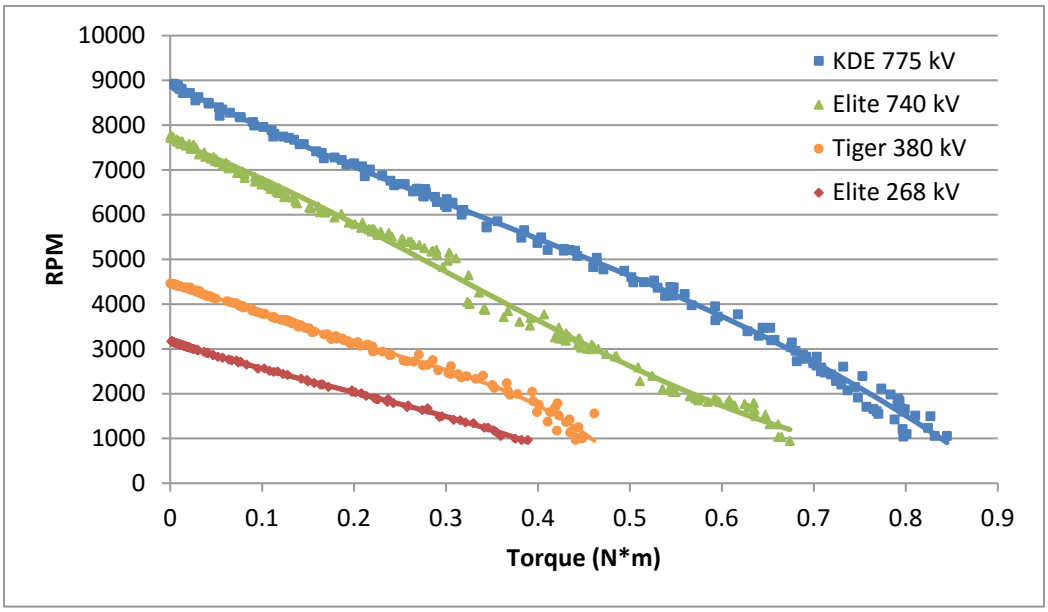

Figure 24. RPM-Torque Comparison of Motors with Various Kv ratings at 12V

6.3. Motor Size Comparison

Motor size comparisons are more difficult for commercial motors. Generally, as motors get larger, their Kv ratings get smaller. This is because larger motors are generally more powerful and optimized for high voltage operations. To correct for this, 3 different sized motors with different Kv ratings were tested to ascertain the effects of motor sizing. To compensate for the different Kv ratings of the motors, each motors was run at a voltage that would produce a no-load RPM of exactly 8000 RPM. For example, for a motor whose Kv rating is $Kv = 268\ Kv$, the voltage it would be tested at would calculated using equation {26}.

$$V_{test} = \frac{RPM}{Kv} = \frac{8000}{268} = 30.7V \qquad \{27\}$$

This synthetically corrected all the tested motors to have the same Kv and isolate the effects of motor size. The data from experiments following this scheme is shown in Figure 26. As expected, for motor with the same Kv ratings, that larger motors are more powerful than the smaller motors.

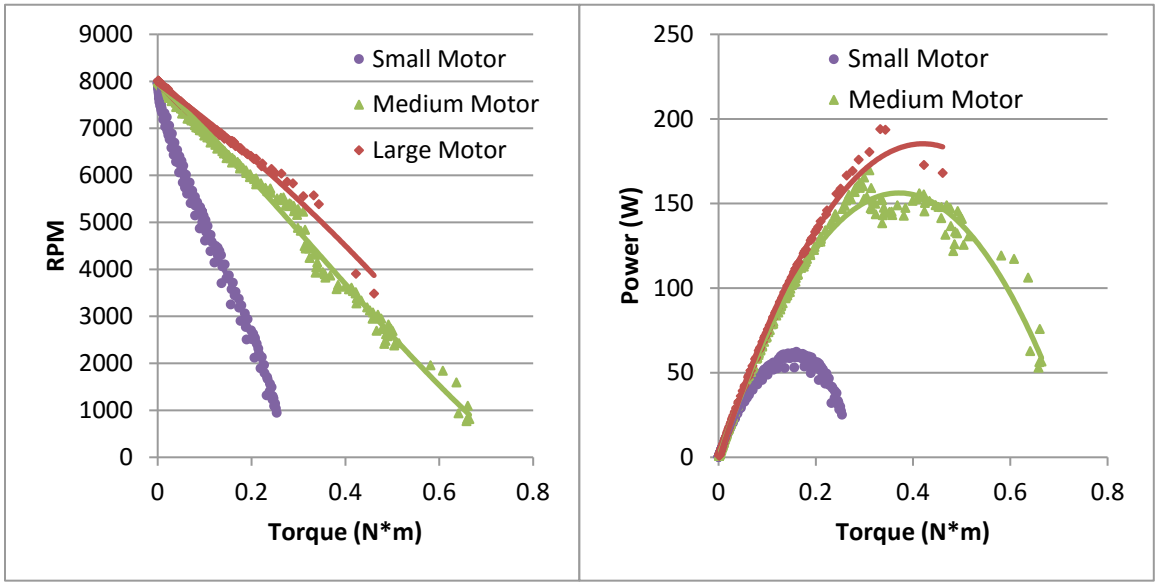

Figure 26. Effects of Motor Size on RPM - Torque and Power - Torque Curves